



Constraints on the numerical age of the Paleocene-Eocene boundary

Adam J. Charles

*School of Ocean and Earth Science, National Oceanography Centre, University of Southampton,
European Way, Southampton SO14 3ZH, UK (a.charles@noc.soton.ac.uk)*

Daniel J. Condon

NERC Isotope Geoscience Laboratory, British Geological Survey, Keyworth NG12 5GG, UK

Ian C. Harding, Heiko Pälike, and John E. A. Marshall

*School of Ocean and Earth Science, National Oceanography Centre, University of Southampton,
European Way, Southampton SO14 3ZH, UK*

Ying Cui and Lee Kump

Department of Geosciences, Pennsylvania State University, University Park, Pennsylvania 16802, USA

Ian W. Croudace

*School of Ocean and Earth Science, National Oceanography Centre, University of Southampton,
European Way, Southampton SO14 3ZH, UK*

[1] Here we present combined radioisotopic dating (U-Pb zircon) and cyclostratigraphic analysis of the carbon isotope excursion at the Paleocene-Eocene (P-E) boundary in Spitsbergen to determine the numerical age of the boundary. Incorporating the total uncertainty from both radioisotopic and cyclostratigraphic data sets gives an age ranging from 55.728 to 55.964 Ma, within error of a recently proposed astronomical age of ~55.93 Ma. Combined with the assumption that the Paleocene Epoch spans twenty-five 405 kyr cycles, our new age for the boundary suggests an age of ~66 Ma for the Cretaceous-Paleogene boundary. Furthermore, our P-E boundary age is consistent with the hypothesis that the onset of the Paleocene-Eocene thermal maximum at the boundary occurred on the falling limb of a 405 kyr cycle, suggesting the event was initiated by a different mechanism to that which triggered the other early Eocene hyperthermals.

Components: 11,800 words, 10 figures.

Keywords: Paleocene; Eocene; PETM; cyclostratigraphy; radioisotopic dating; Spitsbergen.

Index Terms: 1708 History of Geophysics: Geochronology; 1115 Geochronology: Radioisotope geochronology.

Received 4 November 2010; **Revised** 15 March 2011; **Accepted** 4 April 2011; **Published** 7 June 2011.

Charles, A. J., D. J. Condon, I. C. Harding, H. Pälike, J. E. A. Marshall, Y. Cui, L. Kump, and I. W. Croudace (2011), Constraints on the numerical age of the Paleocene-Eocene boundary, *Geochem. Geophys. Geosyst.*, 12, Q0AA17, doi:10.1029/2010GC003426.

Theme: EarthTime: Advances in Geochronological Technique

Guest Editors: D. Condon, G. Gehrels, M. Heizler, and F. Hilgen

1. Introduction

[2] The early Cenozoic was an interval of globally warm climate [e.g., *Zachos et al.*, 2001, 2008; *Pearson et al.*, 2007; *Sluijs et al.*, 2008; *Bijl et al.*, 2009], punctuated by a series of short-term global-scale transient warming events known as hyperthermals [*Kennett and Stott*, 1991; *Zachos et al.*, 2001, 2008; *Cramer et al.*, 2003; *Lourens et al.*, 2005; *Nicolo et al.*, 2007; *Agnini et al.*, 2009; *Galeotti et al.*, 2010]. The most pronounced hyperthermal, the Paleocene-Eocene thermal maximum (PETM), reflects global-scale warming of both surface and bottom waters by $\sim 5^{\circ}\text{C}$ [*Kennett and Stott*, 1991; *Zachos et al.*, 2003; *Tripati and Elderfield*, 2005; *Sluijs et al.*, 2006]. Negative carbon isotope excursions (CIEs) and carbonate dissolution horizons have been shown to be coeval with warming during both the PETM and other hyperthermals [*Lourens et al.*, 2005; *Zachos et al.*, 2005, 2010], implying that a significant quantity of isotopically light carbon was injected into the exogenic system to cause the observed warming [*Dickens et al.*, 1995, 1997; *Sluijs et al.*, 2007; *Panchuk et al.*, 2008; *Zeebe et al.*, 2009]. However, the trigger mechanism for carbon release at the PETM is controversial, with several hypotheses proposed (see *Sluijs et al.* [2007] for a review). Several authors have suggested that insolation maxima during the peak of 100 and 405 kyr eccentricity cycles resulted in warming of oceanic deep waters, causing the dissociation of methane hydrates, thus instigating the warming event(s) [*Cramer et al.*, 2003; *Lourens et al.*, 2005; *Sluijs et al.*, 2007]. Conversely it has also been suggested that the methane and carbon dioxide which initiated the PETM were generated from contact metamorphism of organic-rich sediments around intrusions in North Atlantic sedimentary basins [*Svensen et al.*, 2004, 2010; *Storey et al.*, 2007]; a trigger requiring no orbital forcing but coeval magmatism. An understanding of the causative mechanism(s) for the PETM and later Eocene hyperthermals therefore requires a precise and accurate temporal framework within which the various records can be integrated in order to assess potential drivers (geologic and/or astronomical). Much progress has been made through the construction of high-resolution proxy and lithologic records from various OPD and IODP sites [*Zachos et al.*, 2001, 2003, 2005, 2008; *Sluijs et al.*, 2007, 2008], and the construction of orbitally tuned timescales for these intervals have helped elucidate the relative timing/sequencing of different events [*Lourens et al.*, 2005; *Westerhold et al.*, 2007, 2009;

Westerhold and Röhl, 2009; *Galeotti et al.*, 2010]. However, an outstanding issue relates to the numerical age of key events, such as the PETM, which are currently considered to be “floating,” i.e., the age models contain only relative ages with respect to certain stratigraphic markers. This issue is the result of four factors: (1) the “unstable” nature of the astronomical solutions in the early Paleogene, meaning that numerical ages derived from tuning geological data sets to astronomical solutions carry high uncertainty [*Laskar et al.*, 2004], (2) a gap in cyclostratigraphic records in the middle Eocene, meaning composite cyclostratigraphic records for the entire Eocene cannot currently be constructed [*Hilgen*, 2008; *Pälike and Hilgen*, 2008], (3) disagreement surrounding the length of the Paleocene Epoch as derived from floating cyclostratigraphic timescales, with the presence of either twenty-four or twenty-five 405 kyr eccentricity cycles proposed [*Kuiper et al.*, 2008; *Westerhold et al.*, 2008, 2009; *Hilgen et al.*, 2010], and (4) a lack of geologically well constrained radioisotopic dates, for both the P-E and Cretaceous-Paleogene (K-Pg) boundaries and associated magnetochrons. This is largely a result of uncertainty in the $^{40}\text{Ar}/^{39}\text{Ar}$ dating methods [*Kuiper et al.*, 2008; *Renne et al.*, 2010; *Channell et al.*, 2010] that are used to underpin Cenozoic timescales (note this uncertainty also prevents the accurate determination of the number of 405 kyr cycles in the Paleocene).

[3] The current astronomical solutions are unstable prior to ~ 40 Ma owing to the chaotic nature of the orbits [*Laskar*, 1999; *Varadi et al.*, 2003; *Laskar et al.*, 2004; *Pälike et al.*, 2004]; therefore, unlike the Neogene timescale, construction of a numerical geologic timescale for the Paleogene relies on radioisotopic dating (primarily $^{40}\text{Ar}/^{39}\text{Ar}$ and/or U-Pb) of minerals (sanidine and/or zircon) from volcanic ash layers [e.g., *Wing et al.*, 2000; *Luterbacher et al.*, 2004]. Time series analysis of various proxy records (color, elemental, isotopic) permits identification of cyclicity within sedimentary records that can be attributed to orbital (Milankovitch) forcing, which has permitted the development of floating timescales for the early Paleogene [*Lourens et al.*, 2005; *Westerhold et al.*, 2007, 2008, 2009; *Westerhold and Röhl*, 2009; *Galeotti et al.*, 2010]. Such floating timescales can be constrained via radioisotopic dating of minerals from volcanic layers, either directly or by correlation (using biostratigraphy and/or magnetostratigraphy). At present $^{40}\text{Ar}/^{39}\text{Ar}$ dates underpin much of the Cenozoic timescale. However, the accuracy of these dates is relative to ages of the mineral standard used in

their calibration, typically the Fish Canyon sanidine (FCs) standard, in addition to the potassium decay constants [Renne *et al.*, 1998], both of which have been the focus of ongoing research. Attempts to calibrate the age of FCs using sanidines from multiple tuff layers with both $^{40}\text{Ar}/^{39}\text{Ar}$ and astronomical ages, has resulted in an age of 28.201 ± 0.046 Ma [Renne *et al.*, 1998; Kuiper *et al.*, 2008]. Renne *et al.* [2010] derive an age of 28.305 ± 0.036 Ma for the FCs based upon a data set of paired $^{238}\text{U}/^{206}\text{Pb}$ (zircon) and $^{40}\text{Ar}/^{39}\text{Ar}$ (sanidine and biotite) dates for rocks where the minerals should give equivalent dates. Furthermore, Channell *et al.* [2010] used astronomical ages for Quaternary magnetic reversals, also dated by $^{40}\text{Ar}/^{39}\text{Ar}$, to derive an age of ~ 27.93 Ma for the FCs. These age estimates for the FCs do not overlap within their quoted uncertainties, and combined indicate that the accuracy of $^{40}\text{Ar}/^{39}\text{Ar}$ dates is (at present) limited to $\sim 1\%$. In contrast, the accuracy of U-Pb dates is relative to isotopic tracers which can be accurately calibrated to SI units, and the decay constants that are known through counting experiments [Jaffey *et al.*, 1971]. Precise isotope ratio determinations can therefore result in $^{238}\text{U}/^{206}\text{Pb}$ (zircon) dates with total uncertainties of $<0.2\%$ [Jaffey *et al.*, 1971; Condon *et al.*, 2007]. Furthermore, transformation of mineral dates into eruption/stratigraphic dates requires interpretation of mineral date populations and consideration of petrology (i.e., magma chamber processes, mineral closure temperature for retention of isotopes systematics).

[4] Compounding the problem of Paleogene time-scale calibration is the issue that the geological context of radioisotopically dated samples is somewhat uncertain with respect to the proxy records being constrained. As a result, recent numerical ages derived for the P-E boundary using the recalibrated $^{40}\text{Ar}/^{39}\text{Ar}$ radioisotopic data and cyclostratigraphic data sets have yielded inconsistent ages for the boundary [Kuiper *et al.*, 2008; Westerhold *et al.*, 2008, 2009], preventing consensus on the duration of the Paleocene epoch and the exact temporal relationship of the PETM to potential geologic/orbital triggers [e.g., Svensen *et al.*, 2004, 2010; Storey *et al.*, 2007]. More robust constraints on the numerical age of the P-E boundary are therefore required in order to (1) constrain the duration of the Paleocene Epoch, to ascertain the number of 405 kyr cycles within it and permit the accurate correlation of IODP, ODP and DSDP cores, (2) anchor currently floating cyclostratigraphic records, and (3) constrain the exact temporal relationship between the PETM and potential triggers.

[5] The P-E boundary is defined at the base of the 2.5–6 ‰ negative CIE [Dupuis *et al.*, 2003], coeval with the PETM. Typically, previous studies have only indirectly derived a numerical age for the P-E boundary [e.g., Wing *et al.*, 2000; Luterbacher *et al.*, 2004; Westerhold *et al.*, 2007, 2008, 2009; Kuiper *et al.*, 2008], owing to the absence of ash layers within the PETM CIE (the exception being Jaramillo *et al.* [2010]; see section 4.1). Here we document a U-Pb (zircon) date from a bentonite layer within the PETM CIE from the Longyearbyen section in the Central Basin of Spitsbergen. We combine this date with cyclostratigraphic data sets, from both the Longyearbyen section [Harding *et al.*, 2011] and core BH9/05 (drilled near Sveagruva, Spitsbergen [Dypvik *et al.*, 2011]), to constrain the age of the P-E boundary.

2. Materials and Methods

2.1. Geological Succession

[6] The study localities are located in the Paleogene Central Basin of Spitsbergen, the largest island in the Svalbard Archipelago, situated on the NW corner of the Barents Shelf (Figure 1) [Dallmann *et al.*, 1999; Harland, 1997]. Harland [1997, and references therein] provides a comprehensive overview of the stratigraphy of the Central Basin and the other Paleogene successions on Spitsbergen. The stratigraphic nomenclature used in this report adheres to that proposed by Dallmann *et al.* [1999]. During the Paleogene Spitsbergen was situated at $\sim 75^\circ\text{N}$ [Harland, 1997], adjacent to the NE corner of Greenland, but with the progressive opening of the northern North Atlantic a predominantly transpressional dextral strike-slip motion between the two continental masses was initiated in the Paleocene (Figure 1) [Bruhn and Steel, 2003]. For the remainder of the Paleogene the Central Basin developed as a subsiding foreland basin [Kellogg, 1975; Helland-Hansen, 1990; Müller and Spielhagen, 1990; Harland, 1997], the sediment shed from the rising West Spitsbergen Orogenic Belt resulting in a thick sedimentary succession (up to 2.5 km [Helland-Hansen, 1990]).

[7] Two sections were studied: the Longyearbyen outcrop section and core BH9/05. At Longyearbyen the PETM lies within the Gilsonryggen Member of the Frysjaodden Formation [Harding *et al.*, 2011], a unit of around 250 m of homogeneous mudstones. A -4 ‰ organic carbon isotope excursion ($\delta^{13}\text{C}_{\text{TOC}}$) is present between 3 and 28 m above the top of the Hollendardalen Formation, with the coeval presence of the PETM diagnostic dinoflagellate cyst *Apectodinium augustum* [Harding *et al.*, 2011].

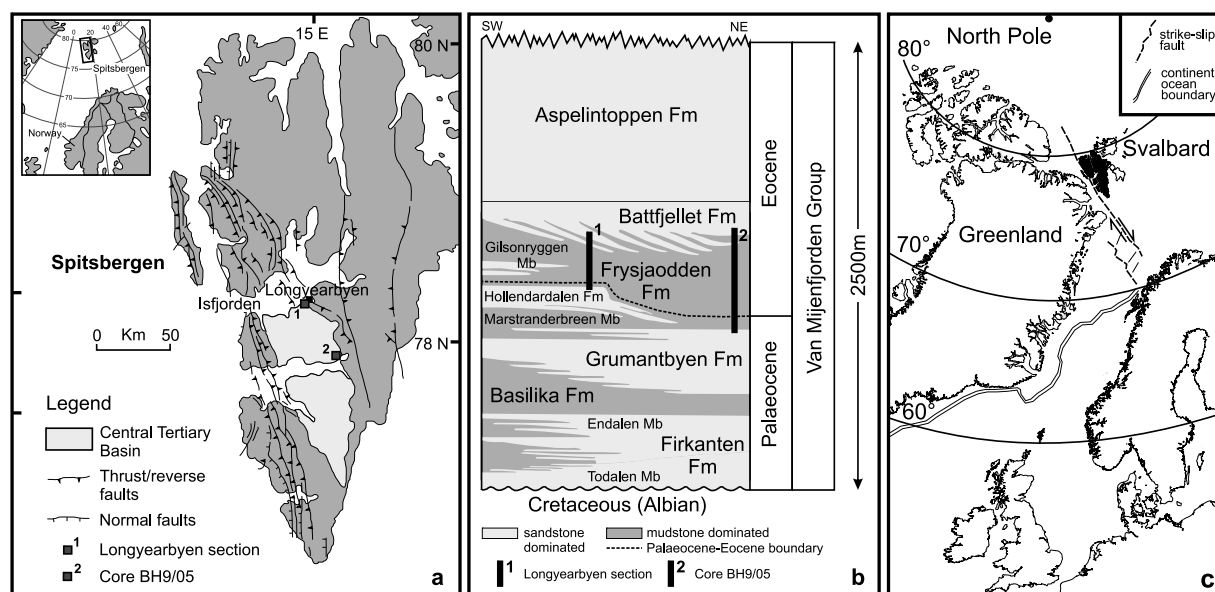


Figure 1. Study area. (a) Map of Spitsbergen illustrating study localities (after Uroza and Steel [2008] and Blythe and Kleinspehn [1998]). (b) The Paleogene stratigraphy of Spitsbergen illustrating the interval of the Frysjaodden Formation studied at each locality (after Uroza and Steel [2008] and Steel *et al.* [1985]). (c) Paleogeographic reconstruction of Spitsbergen (in black) and the Svalbard archipelago in the Eocene (after Mosar *et al.* [2002]).

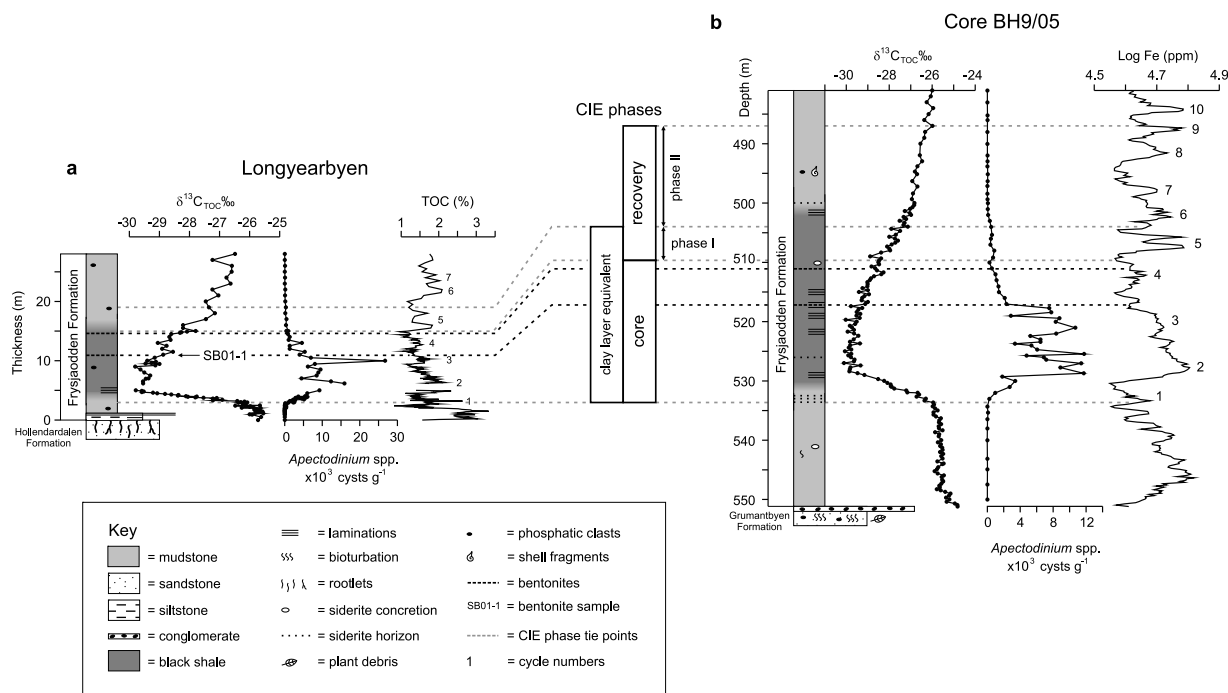


Figure 2. Lithological, dinocyst, and geochemical (organic carbon isotope [$\delta^{13}C_{TOC}$ ‰]; TOC [%]; Log Fe [ppm]) data sets across the P-E boundary from (a) the Longyearbyen outcrop section [Harding *et al.*, 2011] and (b) core BH9/05 (Log: Dypvik *et al.* [2011]; $\delta^{13}C_{TOC}$: Cui [2010]). Note the Hollendardalen Formation is absent in core BH9/05, due to pinch out south of the Longyearbyen section [e.g., Dallmann *et al.*, 1999]. Cycle numbers and CIE phases adhere to those proposed by Röhl *et al.* [2007]. Note that the heights/depths used to define the base and top of recovery phase I are based on analysis of both cyclostratigraphic and $\delta^{13}C_{TOC}$ records (as suggested by Röhl *et al.* [2007]), due to the asymptotic shape of CIE recovery interval in Spitsbergen.

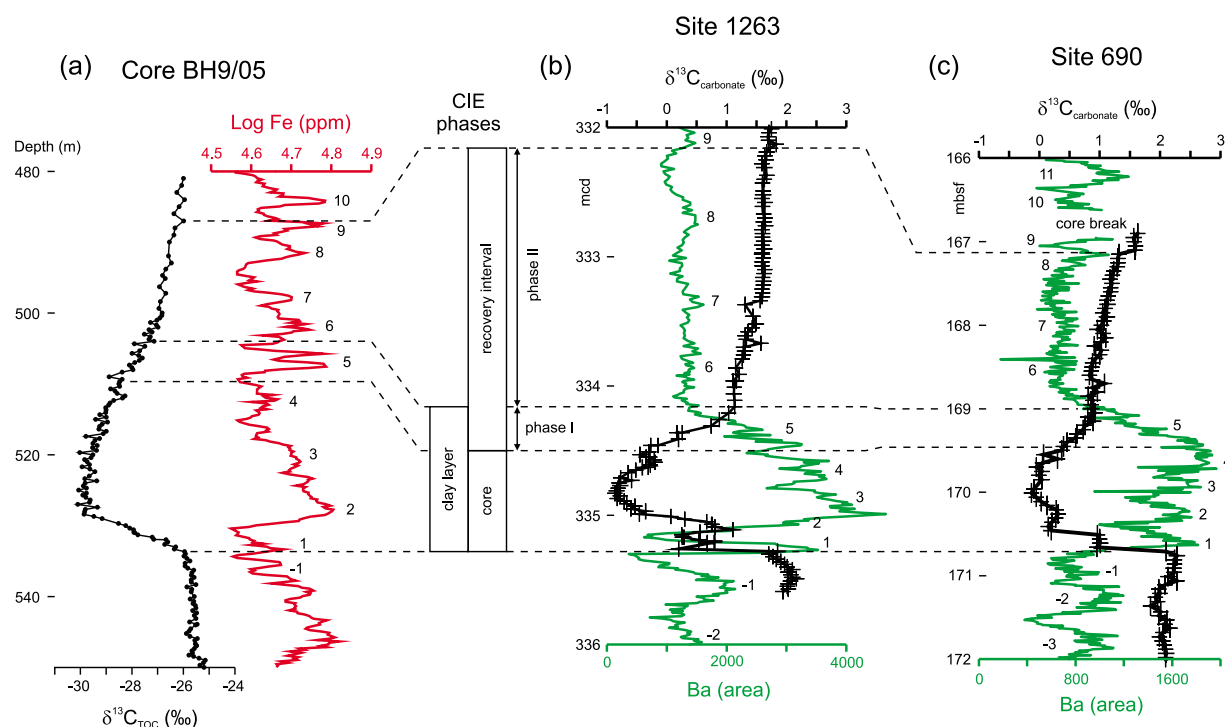


Figure 3. Comparison of PETM CIE records from Spitsbergen and selected ODP sites. (a) Core BH9/05, Spitsbergen, $\delta^{13}\text{C}_{\text{TOC}}$ (‰) record of Cui [2010] (black) and Log Fe (ppm; this study). (b) ODP Site 1263 (Leg 208, Walvis Ridge) $\delta^{13}\text{C}_{\text{carbonate}}$ (‰) record from Zachos *et al.* [2005] (black) and Ba (area) records from Röhl *et al.* [2007] (green). (c) ODP Site 690 (Leg 113, Weddell Sea) $\delta^{13}\text{C}_{\text{carbonate}}$ (‰) record from Bains *et al.* [1999] (black) and Ba records from Röhl *et al.* [2007] (green). Figures 3b and 3c are after Röhl *et al.* [2007]. Cycle numbers and CIE phases adhere to those proposed by Röhl *et al.* [2007]. Note that due to the asymptotic shape of CIE recovery interval in Spitsbergen, we identified the onset and end of recovery phase I using both the $\delta^{13}\text{C}_{\text{TOC}}$ and cyclostratigraphic records of core BH9/05, as suggested by Röhl *et al.* [2007].

Two conspicuous bentonite horizons occur at 10.90 and 14.60 m above the top of the Hollendardalen Formation, within the PETM CIE (Figure 2).

[8] The Frysjaodden Formation is identified from 551 to 110 m depth in core BH9/05 [Dypvik *et al.*, 2011], drilled NW of the town of Sveagruva near Urdkollbreen. The cored succession cannot be divided into members due to the fine grained nature of the lithologies [Dallmann *et al.*, 1999]. The mudstone-dominated succession is continuous across the upper Paleocene–lower Eocene interval, with only minor amounts of carbonate detected in XRD analyses [Dypvik *et al.*, 2011]. A -4.2 ‰ organic carbon isotope ($\delta^{13}\text{C}_{\text{TOC}}$) excursion is present at the base of the Frysjaodden Formation in core BH9/05 (534–487 m depth, see Figure 2 [Cui, 2010]), again coincident with two bentonite horizons lying at 517.20 and 511.10 m depth, respectively [Dypvik *et al.*, 2011].

2.2. Palynological Processing

[9] Sixty-six samples were processed in order to constrain the $\delta^{13}\text{C}_{\text{TOC}}$ excursion in core BH9/05 using

dinoflagellate cyst (dinocyst) biostratigraphy. Sample processing methods were identical to those of Harding *et al.* [2011], with the exception that no samples were subject to ultrasonic treatment. Concentrations of dinocysts were generated by counting 300 specimens where possible, with normalization against the out-of-count *Lycopodium* spike [Stockmarr, 1971]. Dinocyst taxonomy follows that of Fensome and Williams [2004]. The appearance of the dinocyst *Apectodinium augustum* at the start of the $\delta^{13}\text{C}_{\text{TOC}}$ excursion firmly identifies the PETM in core BH9/05, illustrating that the bentonite horizons in both the Longyearbyen section and core BH9/05 are coeval (Figure 2). The PETM CIE from core BH9/05 is plotted in Figure 3 to illustrate the different phases of the CIE in Spitsbergen, with respect to ODP sites 690 and 1263.

2.3. Radioisotopic Dating

[10] Analysis of the lower bentonite layer in the Longyearbyen section (sample SB01-1; Figure 2), was carried out at the NERC Isotope Geosciences Laboratory (NIGL), UK. Zircons were isolated from

around 300 g of sample SB01-1, using conventional mineral separation techniques. Prior to isotope dilution thermal ionization mass spectrometry (ID-TIMS) analyses zircons were subject to a modified version of the chemical abrasion technique [Mattinson, 2005]. For details of sample pretreatment, dissolution and anion exchange chemistry at NIGL the reader is referred to *Sláma et al.* [2008]. Our U-Pb ID-TIMS analyses utilized the EARTHTIME ^{205}Pb - ^{233}U - ^{235}U (ET535) tracer solution. Measurements at the NERC Isotope Geosciences Laboratory were performed on a Thermo Triton TIMS. Pb analyses were measured in dynamic mode on a MassCom SEM detector and corrected for $0.14 \pm 0.04\%$ mass fractionation. Linearity and dead time corrections on the SEM were monitored using repeated analyses of NBS 982, NBS 981 and U500. Uranium was measured in static Faraday mode on 10^{11} ohm resistors or for signal intensities <15 mV, in dynamic mode on the SEM detector. Uranium was run as the oxide and corrected for isobaric interferences with an $^{18}\text{O}/^{16}\text{O}$ composition of 0.00205 (IUPAC value and determined through direct measurement at NIGL). U-Pb dates and uncertainties were calculated using the algorithms of *Schmitz and Schoene* [2007], combined with a $^{235}\text{U}/^{205}\text{Pb}$ ratio of 100.18 and $^{233}\text{U}/^{235}\text{U}$ double spike ratio of 0.99464 for the ET535 tracer. All common Pb in the analyses was attributed to the blank and subtracted based on the isotopic composition and associated uncertainties analyzed over time. The $^{206}\text{Pb}/^{238}\text{U}$ ratios and dates were corrected for initial ^{230}Th disequilibrium using a $\text{Th}/\text{U}_{[\text{magma}]}$ of 4 ± 1 applying the algorithms of *Schärer* [1984] resulting in an increase in the $^{206}\text{Pb}/^{238}\text{U}$ dates of ~ 100 kyr and an additional uncertainty contribution of ~ 10 kyr. Errors for U-Pb dates are reported in the following format: $\pm X(Y)[Z]$, where X is the internal or analytical uncertainty in the absence of all systematic error (tracer calibration and decay constants), Y includes the quadratic addition of tracer calibration error (using a conservative estimate of the 2σ standard deviation of 0.1% for the Pb/U ratio in the tracer), and Z includes the quadratic addition of both the tracer calibration error and additional ^{238}U decay constant errors of *Jaffey et al.* [1971]. All analytical uncertainties are calculated at the 95% confidence interval. These $^{238}\text{U}/^{206}\text{Pb}$ dates are traceable back to SI units via the gravimetric calibration of the EARTHTIME U-Pb tracer and the determination of the ^{238}U decay constant [Jaffey et al., 1971; Condon et al., 2007].

2.4. XRF Time Series

[11] Fe and Mn time series were generated for core BH9/05 using a Niton UK XL3t portable XRF

scanner. Measurements ($n = 1195$; Table S1 in the auxiliary material) were taken every 20 cm throughout that part of the core section recording the $\delta^{13}\text{C}_{\text{TOC}}$ excursion (550 m to 480 m core depth) and every 40 cm outside this interval (Figure 4).¹ Twelve samples were analyzed using wavelength dispersive (WD) XRF, to calibrate results from the Niton UK scanner. These samples were crushed to a fine powder and air dried at 105°C . The sample ($0.5 \text{ g} \pm 0.0003$) was mixed with $5 \pm 0.003 \text{ g}$ lithium tetraborate flux (Fluxana GmbH, Germany) and fused at $\sim 1100^\circ\text{C}$ using a Vulcan fusion system (HD Elektronik und Elektrotechnik GmbH, Germany) to provide a 1:10 glass bead. The glass beads were analyzed using a Philips MAGIX-PRO automatic sequential wavelength dispersive X-ray fluorescence spectrometer fitted with a 4 kW Rh X-ray tube. Loss on ignition (LOI) was estimated from the function ($100\% - \sum \text{XRF oxides}$) since the original XRF major element calibration was constructed on this basis. We obtained correlation coefficients (r^2) between the WD XRF and the Niton UK scanner of 0.76 for Fe and 0.89 for Mn (Figure 5).

2.5. Time Series Analysis

[12] Both Fe and Mn time series were first smoothed using a 5 point moving average in order to reduce noise. Log Fe and Mn values were used in order to stabilize cycle variance, with the data also normalized and detrended before spectral analysis [Weedon, 2003]. Gaussian filtering and tuning were carried out using Analyseries version 1.1 [Paillard et al., 1996]. In order to generate both wavelet and multitaper method power spectra, both Fe and Mn time series were resampled using a constant sample spacing, via linear interpolation using Analyseries. Multitaper method power spectra [Thomson, 1982] were calculated using SSA-MTM toolkit [Dettinger et al., 1995; Ghil et al., 2002] with a red noise model to assess confidence levels. Wavelet spectra were calculated using the Matlab script of Torrence and Compo [1998]. The time series was zero padded to reduce edge effects, with a red noise model to assess confidence levels [Torrence and Compo, 1998].

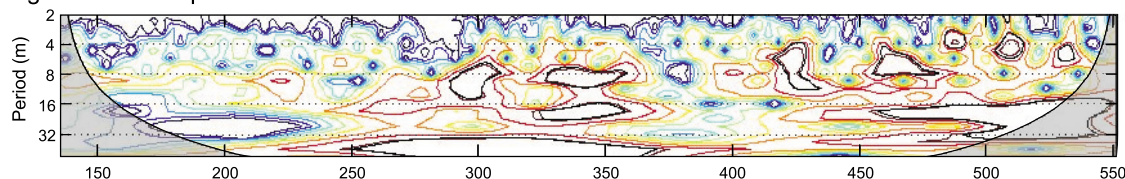
3. Results

3.1. Radioisotopic Dating

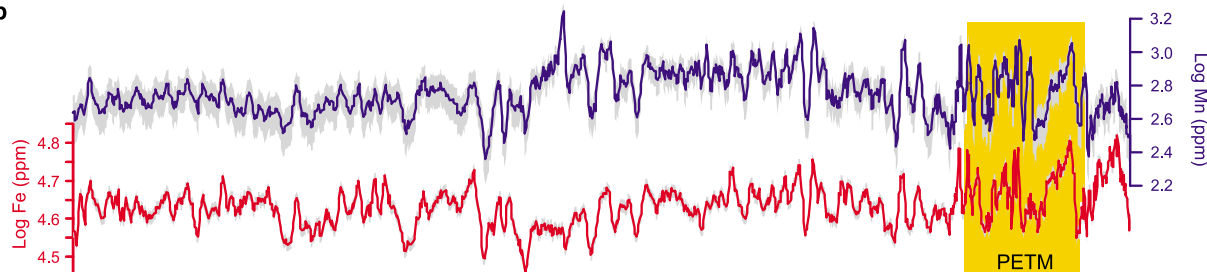
[13] Zircons separated from bentonite sample SB01-1 were small ($<50 \mu\text{m}$) with aspect ratios of

¹Auxiliary materials are available in the HTML. doi:10.1029/2010GC003426.

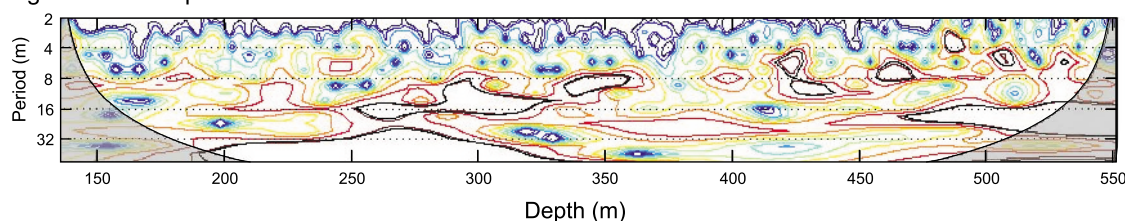
a Log Mn wavelet spectra



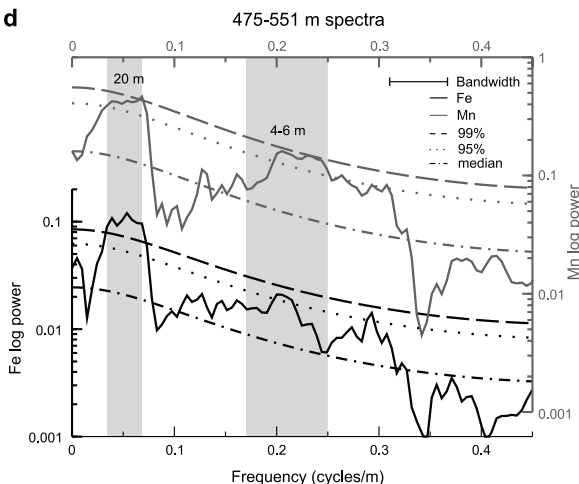
b



c Log Fe wavelet spectra



d



e

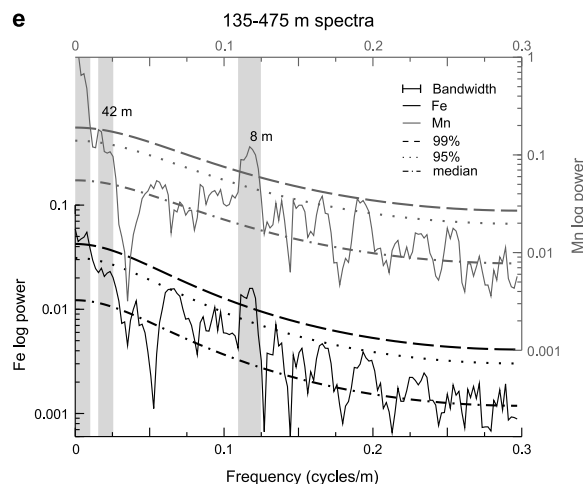


Figure 4. BH9/05 time series in the depth domain. (a, c) Log Mn and Fe wavelet spectra, respectively. Black lines indicate 95% significance level. Shaded area indicates the “cone of influence,” where edge effects make recognition of cycles less confident [Torrence and Compo, 1998]. Warm (cold) colors indicate high (low) spectral power. (b) Log Mn (blue) and Fe (red) time series. Grey bands represent 2σ error values for the precision of the Niton UK XRF scanner, calculated using the standard deviation derived from repeat analyses of 15 samples, each measured 10 times. Yellow box indicates stratigraphic thickness of PETM CIE. (d, e) Multitaper method power spectra [Thomson, 1982] for the intervals from 475 to 551 m and 135 to 475 m, respectively. Grey bars illustrate the dominant cycles and their stratigraphic thickness. Note the wide bandwidth on Figure 4d is the result of the short stratigraphic thickness of the time series with respect to the cycle wavelengths being analyzed (which has the effect of smearing out the spectral peaks). Spectra were generated by resampling the time series using a constant sample spacing (0.2 m, Figure 4d; 0.5 m, Figure 4e), using three tapers. Red noise models were generated using SSA-MTM toolkit [Ghil et al., 2002] to calculate the confidence levels illustrated.

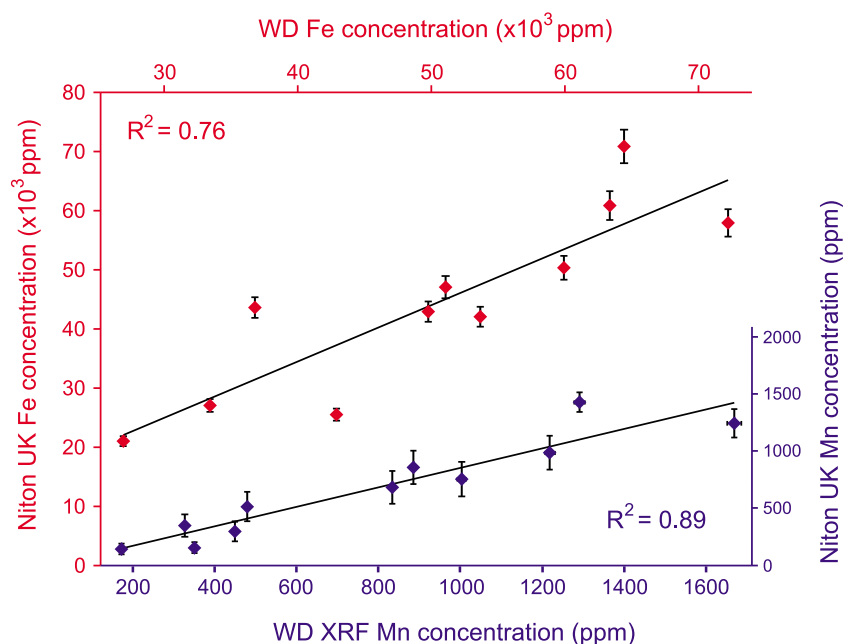


Figure 5. Calibration curve for the Niton UK portable XRF device to wavelength dispersive (WD) XRF.

~3 to ~7. Thirteen single grains were analyzed, and the resulting data are presented in Table S2. Three of the thirteen analysis produced discordant U-Pb data with Paleozoic $^{207}\text{Pb}/^{206}\text{Pb}$ dates. The remaining ten analyses yielded $^{206}\text{Pb}/^{238}\text{U}$ dates between 57.08 and 55.71 Ma (Figure 6). U-Pb ages for volcanic ash beds are determined by the interpretation of U-Pb dates from single zircon crystals. Utilization of the chemical abrasion pretreatment technique [Mattinson, 2005] for the effective elimination of Pb loss means that we consider each zircon $^{206}\text{Pb}/^{238}\text{U}$ date accurate (i.e., they do not reflect postcrystallization Pb loss). Detailed studies of zircons and other minerals dateable by the U-Pb system often indicate a protracted interval of zircon crystallization in a magmatic system, demonstrating the possibility that some zircon in a given ash layer record ages of the eruption (i.e., those that crystallized immediately prior to eruption) and some older ages which reflect the pre-eruptive crystallization (and residence) of zircons [Schoene et al., 2010]. In such samples the age of the youngest zircon (or zircon population) is considered to best approximate the age of the ash layers with older zircon dates reflecting pre-eruptive crystallization. Excluding obvious inheritance of Paleozoic zircon, we observe a range of zircon $^{206}\text{Pb}/^{238}\text{U}$ dates in sample SB01-1 from 57.08 ± 0.06 to 55.71 ± 0.14 Ma, with the five youngest analyses yielding a weighted mean $^{206}\text{Pb}/^{238}\text{U}$ date of $55.785 \pm 0.034(0.066)[0.086]$ Ma (MSWD = 0.88, calculated

using Isoplot 3.0 [Ludwig, 1991]) which is interpreted as being the best estimate for the zircons of this sample. We consider this date to best approximate the age of sample SB01-1 and the older zircon $^{206}\text{Pb}/^{238}\text{U}$ dates to reflect analyses of xenocrystic and/or zircons that have experienced pre-eruptive magma residence, with the single analysis precision of ~100 kyr permitting deconvolution of the mixed age population. An alternative to the conventional approach of taking a weighted mean date based upon a coherent population of youngest $^{206}\text{Pb}/^{238}\text{U}$ dates would be to interpret the single zircon dates. As the youngest five analyses form a coherent population this would have no discernable effect on the interpreted $^{206}\text{Pb}/^{238}\text{U}$ date for SB01-1 and would increase the total uncertainty by an additional ~20 kyr, and as such our proposed date for SB01-1 is insensitive to different approaches to zircon date interpretation.

3.2. Cyclostratigraphic Analysis

[14] A detailed description of the cyclostratigraphic age model for the Longyearbyen section can be found in Harding et al. [2011]. Here, numerical ages from Longyearbyen [Harding et al., 2011] were corrected using the numerical age of the bentonite. However, we also generated Fe and Mn time series from core BH9/05, with cyclostratigraphic analysis of this data discussed below.

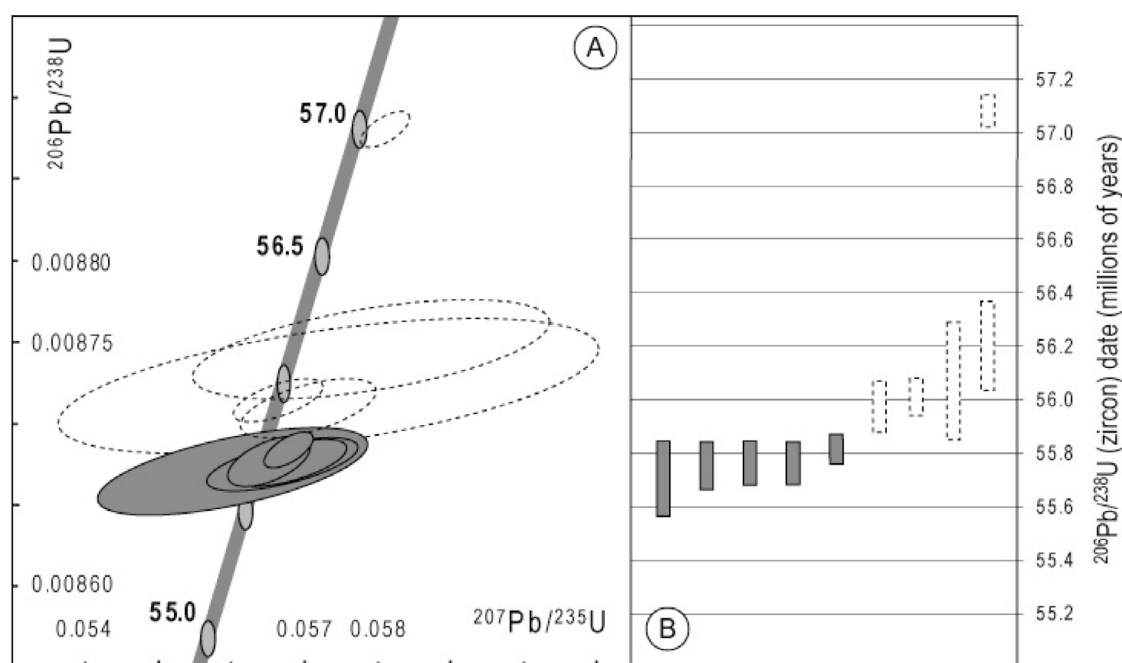


Figure 6. U-Pb data for sample SB01-1. (a) Conventional U-Pb concordia plot of zircons analyzed from sample SB01-1. The gray band reflects the uncertainty in the ^{238}U and ^{235}U decay constants [Jaffey *et al.*, 1971]. (b) Plot of $^{238}\text{U}/^{206}\text{Pb}$ dates for single zircon crystal analyses (same data as in Figure 6a). Dashed ellipses/bars represent analyses of zircon that are considered to be xenocrysts and/or inherited crystals that are disregarded in calculation of final date, whereas gray filled ellipses/bars represent the analyses used for calculation of the weighted mean final date (see text for discussion).

3.2.1. Records in the Depth Domain

[15] In order to build an orbital age model for core BH9/05, it was first necessary to ascertain if the cycles present in the time series were derived from orbital forcing [Weedon, 2003; Bailey, 2009]. Comparison of the Fe/Mn time series of core BH9/05 with the TOC record from Longyearbyen illustrates that the same cycles are present in the depth domain in both different parameters and localities within Spitsbergen (Figure 2). This confirms the cycles present in the PETM are not predominantly the result of stochastic noise [Weedon, 2003].

[16] The BH9/05 time series (Figure 4) illustrate a strong cyclicity within the interval from the base of the Frysjaodden Formation to the top of the PETM (551–487 m), with two dominant cycle lengths of 4–6 m (~ 0.2 cycles/m) and 20 m (0.05 cycles/m) above 95% confidence level (Figure 4; note that the short stratigraphic thickness of this interval with respect to the cycle wavelengths being analyzed results in a wide bandwidth for the power spectra shown in Figure 4d, which has the effect of smearing out the spectral peaks). Above this interval the cycle wavelength increases, with components at 0.12 and 0.024 cycles/m representing 8 m and

42 m cycles, respectively (Figure 4). The wavelet spectra therefore suggest that the sedimentation rate increases above the PETM (as cycle wavelength increases when sedimentation rates rise). This is in contrast to other PETM continental margin sections, which typically show an increase in sedimentation rates within the PETM [e.g., John *et al.*, 2008; Sluijs *et al.*, 2008]. However, the Central Basin lies adjacent to the West Spitsbergen Orogeny, and thus the high volume of sediment shed off the growing orogenic belt at this time [Harland, 1997; Dallmann *et al.*, 1999] probably overprinted any climatically induced changes in sedimentation. The increase in sedimentation rate above the PETM is also consistent with the gradual infilling of the basin through time, eventually leading to deposition of the overlying shelf margin delta and terrestrial formations (Battfjellet and Aspelintoppen Formations, respectively [see Dallmann *et al.*, 1999]).

[17] In order to estimate the duration of the Fe and Mn cycles, an independent estimate of the sedimentation rate is required. Outside the PETM interval, no such constraints are currently available. Therefore, the rest of this study will focus on the interval between the base of the Frysjaodden

Formation and the end of the PETM (551–487 m), where the PETM CIE acts as an external constraint on cycle durations. Note that the PETM CIE is a valid external constraint for the following reasons: (1) the CIE inflection points in $\delta^{13}\text{C}_{\text{TOC}}$ and $\delta^{13}\text{C}_{\text{n-alkane}}$ records in core BH9/05 are at stratigraphically equivalent heights [Cui, 2010], indicating changes in organic matter assemblage did not alter the stratigraphic position of the CIE inflection points, and (2) the abundance of reworked pre-Cenozoic palynomorphs is low throughout the lower Frysjaodden Formation [Harding et al., 2011], indicating reworking of such material did not significantly alter the $\delta^{13}\text{C}_{\text{TOC}}$ record. Furthermore, the consistent stratigraphy between Spitsbergen sites (Figure 2) suggests localized reworking of Paleocene organic matter did not significantly affect our records (as differential reworking of isotopically heavy pre-PETM material would alter the carbon isotope stratigraphy between sites [Harding et al., 2011]).

[18] The stratigraphic thickness of the PETM CIE in core BH9/05 (onset to the end of recovery phase II: 533.66 m to 487.00 m) was combined with previously published data for the duration of this interval to calculate the sedimentation rate during the PETM. However, different estimates for the duration of the PETM CIE currently exist. Röhl et al. [2007] used cycles in Fe, Ca and Ba at ODP sites 1263 (Walvis Ridge) and 690 (Weddell Sea) to derive a PETM duration of 170 kyr (8.5 precession cycles), which is similar to cyclostratigraphic results from the Bighorn Basin (157 kyr, 7.5 precession cycles [Abdul Aziz et al., 2008]). A recent reappraisal of the ^3He age model of Farley and Eltgroth [2003] led to estimates from 90 ± 10 to 140 ± 30 kyr for the duration of the PETM CIE at ODP Site 690 [Sluijs et al., 2007], with the upper estimate consistent with recent cyclostratigraphic results. As similar durations for the PETM CIE have been derived from both low (Walvis Ridge), mid (Bighorn Basin) and high (Weddell Sea) latitudes it is reasonable to assume that the duration of the event would have been the similar in the Arctic (170 kyr, following Röhl et al. [2007]). Given the 46.6 m thickness of the CIE (Figure 2) and assuming that its duration is 170 kyr yields a sedimentation rate of 27.4 cm/kyr (4660 cm/170 kyr). Using this sedimentation rate the 4–6 m and 20 m cycles within the PETM represent 15–22 kyr and 73 kyr cycles, respectively.

[19] However, recently Murphy et al. [2010] derived a duration of $217 +44/-31$ kyr for the PETM CIE (onset to the end of recovery phase II) from ODP

Site 1266 using an extraterrestrial ^3He age model. Potential reasons for the difference between this age model and that of Röhl et al. [2007] were previously discussed in Murphy et al. [2010]. Using a duration of 217 kyr for the PETM CIE (onset to the end of recovery phase II) together with the stratigraphic thickness of the same interval from core BH9/05 gives sedimentation rates of 21.5 cm/kyr (4660 cm/217 kyr). In this scenario, the 4–6 m and 20 m cycles would have durations of 19–28 kyr and 93 kyr, respectively. The duration of the 4–6 m cycles using either the Röhl et al. [2007] or Murphy et al. [2010] age models is therefore consistent with their derivation from precession forcing. The ratio between the 4–6 and 20 m cycles suggests the 20 m cycle represents the short eccentricity component (~ 100 kyr), consistent with the cycle duration derived using the Murphy et al. [2010] age model. The dominance of precession and eccentricity with a minor obliquity component in late Paleocene/early Eocene sediments is typical and has been observed at numerous sites on a global scale [e.g., Westerhold et al., 2007, 2008; Abdul Aziz et al., 2008; Sluijs et al., 2008].

[20] Because of the different age models for the duration of the PETM CIE, we present two options for the interpretation of the cycles within core BH9/05 (section 3.2.2). We extracted the Gaussian filter outputs from the Fe and Mn time series in the depth domain at wavelengths of 4.2 m (0.24 ± 0.07 cycles/m), and 20 m (0.05 ± 0.01 cycles/m; Figure 7). The 4.2 m and 20 m filters represent the precession and short eccentricity components, respectively, with precession cycles numbered according to Röhl et al. [2007]. Figure 7 shows that a minimum of 8.5 precession cycles are present within the PETM CIE (from onset to end of recovery phase II), consistent with the cyclostratigraphic age model of Röhl et al. [2007]. If we consider the Röhl et al. [2007] age model to be the most accurate, the precession cycles labeled 1 to 3 in Figure 7 (i.e., excluding those marked with an asterisk) correspond to one short eccentricity (20 m) cycle. However, between 4 and 6 precession cycles (typically 5) should be present for every short eccentricity cycle [e.g., Pälike, 2005], and thus it is difficult to reconcile the two filter outputs in this interval. Furthermore, we identify three additional cycles with low amplitude in the time series and filter outputs in the PETM interval (marked with asterisks) when compared to the Röhl et al. [2007] age model (Figure 7). If these cycles are interpreted as low-amplitude precession cycles, the duration of the PETM CIE is consistent

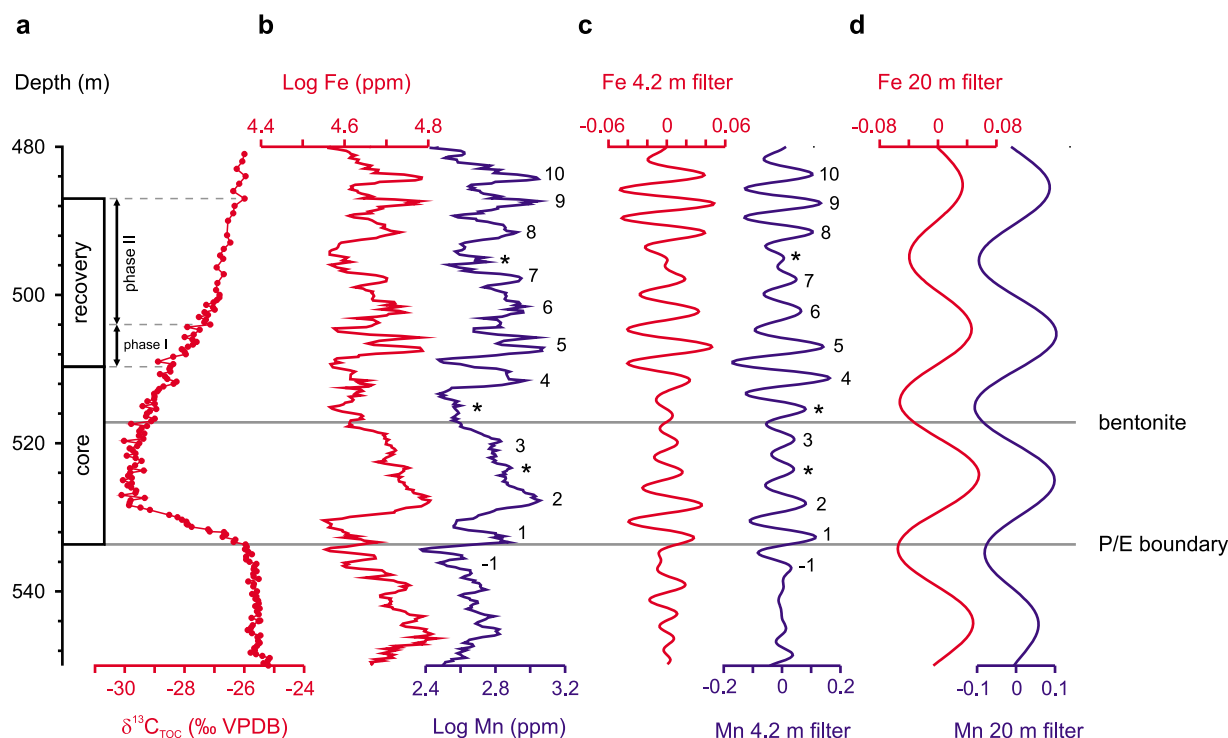


Figure 7. Filtered records of core BH9/05 in the depth domain. (a) The $\delta^{13}\text{C}_{\text{TOC}}$ (‰) from Cui [2010], illustrating the phases of the PETM CIE from Röhl *et al.* [2007]. (b) BH9/05 Log Fe (ppm; red) and Mn (ppm; blue) time series. Cycle numbers adhere to those of Röhl *et al.* [2007], with potential additional cycles marked with an asterisk. (c) Log Fe (red) and Log Mn (blue) 4.2 m (0.24 ± 0.07 cycles/m) Gaussian filter output, representing the precession component of orbital forcing (cycle numbers as in Figure 7b). (d) Log Fe (red) and Log Mn (blue) 20 m (0.05 ± 0.01 cycles/m) filter, representing the short eccentricity (~ 100 kyr) component of orbital forcing.

with that obtained from the ^3He age model of Murphy *et al.* [2010], i.e., 11 precession cycles. Using this approach the short eccentricity:precession cycle ratio is 1:5, consistent with orbital cycle ratios [e.g., Pälike, 2005]. Two of the additional precession cycles occur within the interval between the PETM CIE onset and the end of recovery phase I (making a total of 7 cycles; Figure 7), which is equivalent to the clay layer interval in ODP Leg 208 sites (Figure 3). This is consistent with the hypothesis of Röhl *et al.* [2007], who argued that 5–7 precession cycles must be present within the clay layer interval of Leg 208 sites, in order to maintain the phase of the 405 kyr eccentricity cycle extracted from Site 1262.

3.2.2. Records in the Time Domain

[21] Here we construct two separate cyclostratigraphic age models for core BH9/05 (from 551 to 487 m), each based on the different options for the duration of the PETM CIE from Röhl *et al.* [2007] and Murphy *et al.* [2010]. Option A, matching the

BH9/05 records to the Röhl *et al.* [2007] age model, was carried out by matching the Fe concentration record from BH9/05 to that of ODP Leg 208, Site 1263 ([Westerhold *et al.*, 2007] corrected after Röhl *et al.* [2007]) (Table S4), using the PETM CIE as an external constraint. The duration of the PETM CIE from the ^3He age model of Murphy *et al.* [2010] is longer than recent cyclostratigraphic estimates of the PETM CIE [e.g., Röhl *et al.*, 2007; Abdul Aziz *et al.*, 2008], and therefore tuning the BH9/05 record to another site consistent with this ^3He age model is currently not possible. Therefore, in order to build an age model for core BH9/05 consistent with the results of Murphy *et al.* [2010], we assigned a 21 kyr duration to the interval between each precession cycle peak, for each cycle identified in the filter output of Figure 7c (following a similar approach by Westerhold *et al.* [2007] and Röhl *et al.* [2007]). Note that this approach assumes sedimentation rates remained constant between precession cycle peaks. Cycle peaks were assigned ages relative to cycle –1 in Figure 7c, with the resultant age model (option B) shown in Table S4. However, we note that preces-

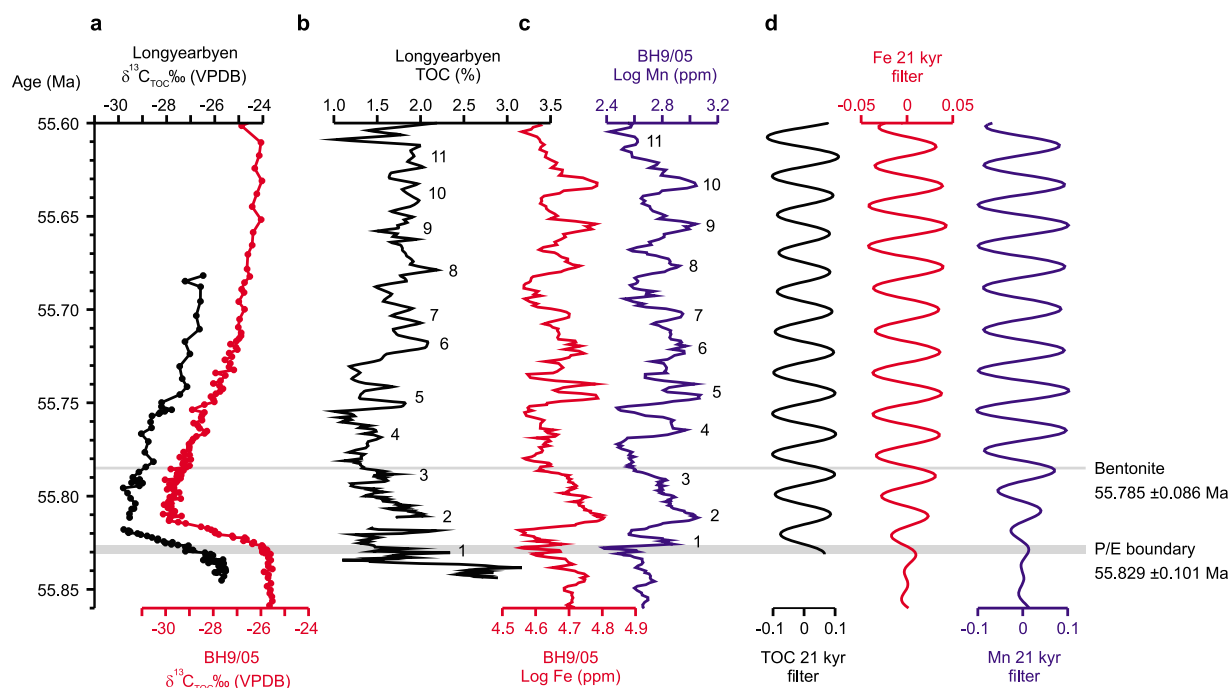


Figure 8. The age of the Paleocene-Eocene boundary in Spitsbergen, using cyclostratigraphic option A. (a) The $\delta^{13}\text{C}_{\text{TOC}}$ (‰) from the Longyearbyen section (black) [Harding *et al.*, 2011] and core BH9/05 (red) [Cui, 2010]. (b) Longyearbyen TOC (%) [Harding *et al.*, 2011]. (c) Core BH9/05 Log Fe (ppm, red) and Mn (ppm, blue). (d) Twenty-one kyr Gaussian filter outputs for TOC (black) Log Fe (red) and Log Mn (blue), respectively, illustrating an ~40 kyr duration between the onset of the PETM CIE and the bentonite layer.

sion cyclicity is quasiperiodic, with cycle durations ranging from 19 to 24 kyr in duration [e.g., Pälike, 2005]. Therefore, we estimate an error of ± 3 kyr for each precession cycle peak utilized in age model option B.

3.3. The Numerical Age of the Paleocene-Eocene Boundary

[22] The P-E boundary is defined as the base of the PETM CIE [Dupuis *et al.*, 2003] and we therefore integrate the age of the bentonite with time series data sets to constrain the age of the P-E boundary (and by inference the onset age for the PETM CIE). Numerical ages for both the cyclostratigraphic age models from section 3.2.2 and the record from the Longyearbyen section [Harding *et al.*, 2011] were corrected using the age of the bentonite. In order to constrain the age of the P-E boundary, the relative duration between the dated bentonite horizon and the onset of the PETM CIE is required. No grain size fluctuations or abrupt shifts in carbon isotope values were observed within this interval in either the Longyearbyen section or core BH9/05 (Figure 2), implying that sedimentation was continuous between the onset of the CIE and the lower bentonite horizon.

[23] Figure 8 shows the duration between the bentonite and base of the PETM CIE using age model option A for core BH9/05 together with the cyclostratigraphic age model from the Longyearbyen section [Harding *et al.*, 2011]. Cycle counting using the Gaussian filter output of precession illustrates a 40 and 45 kyr duration between the lower bentonite and the base of the PETM CIE in core BH9/05 and at Longyearbyen, respectively, which results in numerical ages of 55.827 ± 0.086 Ma (BH9/05) and 55.831 ± 0.086 Ma (Longyearbyen) for the P-E boundary (Figure 8). As each section was tuned independently, the 5 kyr difference between the ages derived from each section partly represents the error associated with the tuning process. However, as the time series from each section are constructed from different parameters (TOC% in Longyearbyen; Fe and Mn concentrations in core BH9/05), part of the 5 kyr offset may result from differences in how the individual parameters were incorporated into the sedimentary record. Therefore, we incorporate the 5 kyr offset into the error for the age the P-E boundary. Further error results from tuning the cyclostratigraphic records from Spitsbergen to the Fe record of ODP Site 1263, because carbonate dissolution at the base of the

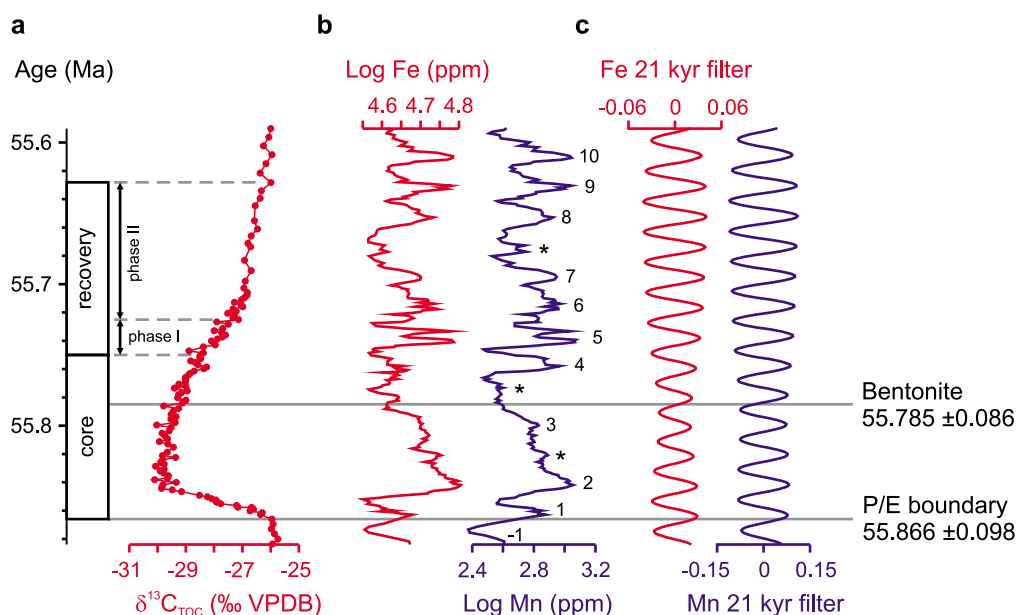


Figure 9. The age of the Paleocene-Eocene boundary in Spitsbergen, using cyclostratigraphic option B. (a) The $\delta^{13}\text{C}_{\text{TOC}}$ (‰) from core BH9/05 (red) [Cui, 2010], illustrating the phases of the PETM CIE from Röhl *et al.* [2007]. (b) Core BH9/05 Log Fe (ppm, red) and Mn (ppm, blue). Cycle numbers adhere to those of Röhl *et al.* [2007], with potential additional cycles marked with an asterisk. (d) Twenty-one kyr Gaussian filter outputs for Log Fe (red) and Log Mn (blue), respectively, illustrating an ~80 kyr duration between the onset of the PETM CIE and the bentonite layer.

PETM clay layer at Site 1263 results in a minor hiatus in this section [Zachos *et al.*, 2005; McCarren *et al.*, 2008]. It is estimated that the duration of missing time owing to carbonate dissolution is on the order of 10 kyr [Röhl *et al.*, 2007], which we incorporate into the error, producing an age of 55.829 ± 0.101 Ma (Figure 8). Conversely, using age model option B for core BH9/05 results in a duration of 81 kyr between the bentonite and the base of the PETM CIE (Figure 9), giving an age of 55.866 ± 0.098 Ma for the P-E boundary. The error based on age model option B includes ± 0.086 Myr from U-Pb dating of bentonite SB01-1, and ± 0.012 Myr error from cycle counting (4 precession cycles at ± 3 kyr per cycle; section 3.2.2). Note that no error for carbonate dissolution is applied to option B because this approach required no tuning to Site 1263, and the near absence of carbonate in the Frysjaodden Formation [Dypvik *et al.*, 2011; Harding *et al.*, 2011] implies that carbonate dissolution did not alter the Spitsbergen PETM records. The difference between age model option A and B for the age of the P-E boundary is thus ~37 kyr, and both options are within error of one another because the accuracy of the radioisotopic date dominates the uncertainty of our derived P-E boundary age. Therefore, the age of the boundary inferred here is not significantly altered

by large changes in the duration of the PETM CIE used to derive the respective age models. Taking into account both the cyclostratigraphic options and their uncertainty, together with the uncertainty from the radioisotopic dating of sample of SB01-1, we derive an age range of 55.728–55.964 Ma for the P-E boundary (Figure 10).

4. Discussion

4.1. Comparison With Recent Age Estimates for the P-E Boundary

[24] Owing to the lack of direct radioisotopic dating of the P-E boundary (other than Jaramillo *et al.* [2010], see below), earlier studies have derived numerical ages indirectly using either astronomical solutions and/or cycle counting from stratigraphic horizons which are themselves constrained by radioisotopic dating. Three different astronomical age options have recently been proposed for the P-E boundary [Westerhold *et al.*, 2007, 2008]. These options were derived by extracting the 405 kyr cycle from both Fe and a^* records from ODP Site 1262 (Leg 208, Walvis Ridge [Westerhold *et al.*, 2007]). Combined with broad radioisotopic age constraints the correlation of the extracted 405 kyr cycle to astronomical solutions [Varadi

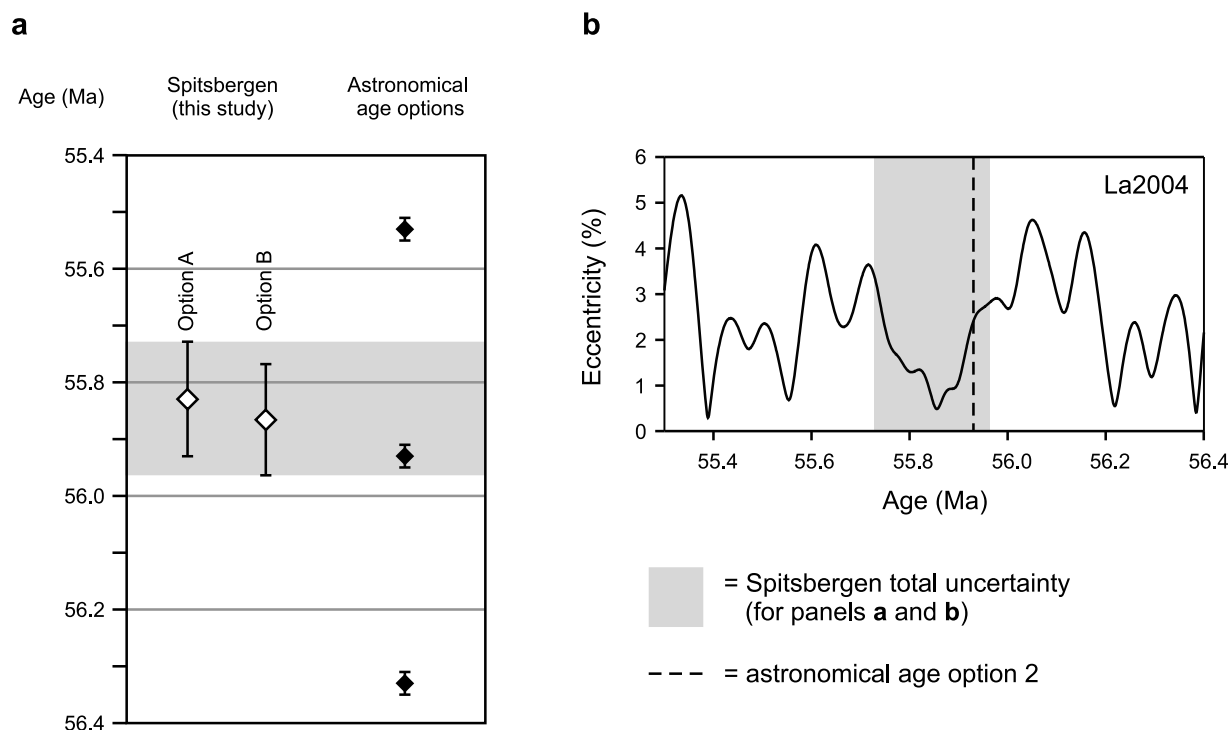


Figure 10. The position of the P-E boundary (equivalent to the PETM CIE onset) with respect to orbital forcing. (a) Comparison of P-E boundary ages determined from Spitsbergen with the astronomical age options of *Westerhold et al.* [2007, 2008]. Note that both Spitsbergen age options are within error of astronomical age option 2 (55.93 Ma). (b) Total uncertainty for the age of the P-E boundary from Spitsbergen (gray shaded bar), plotted against the *Laskar et al.* [2004] (La2004) orbital solution. Age option 2 of *Westerhold et al.* [2007, 2008] is plotted for comparison.

et al., 2003; *Laskar et al.*, 2004] yields three different options each separated by one 405 kyr cycle (option one: ~55.53 Ma; option two: ~55.93 Ma; option three: ~56.33 Ma). Note that three options were proposed due to the uncertainties associated with both astronomical solutions and $^{40}\text{Ar}/^{39}\text{Ar}$ radioisotopic dating [*Westerhold et al.*, 2007, 2008]. The error associated with each option is ± 20 kyr [*Westerhold et al.*, 2007], derived from the error associated with the extremely stable 405 kyr eccentricity cycle as calculated from astronomical modeling [*Laskar et al.*, 2004].

[25] Recent ages for the P-E boundary derived via cycle counting from radioisotopic horizons have utilized $^{40}\text{Ar}/^{39}\text{Ar}$ (sanidine) dating of the K-Pg boundary [*Kuiper et al.*, 2008; *Westerhold et al.*, 2008; *Hilgen et al.*, 2010], and ash -17 in the Fur Formation of Denmark [*Storey et al.*, 2007; *Westerhold et al.*, 2009]. As outlined in section 1, the ~1% uncertainty in the age of the FCs, against which the $^{40}\text{Ar}/^{39}\text{Ar}$ dates are determined, has precluded a high accuracy (<0.2%) age estimate for the P-E boundary using this method. Together with the uncertainty for the duration of the Paleocene Epoch

from floating cyclostratigraphic timescales [*Kuiper et al.*, 2008; *Westerhold et al.*, 2008; *Hilgen et al.*, 2010], this can therefore account for the difference between our age estimate and those recently derived utilizing $^{40}\text{Ar}/^{39}\text{Ar}$ dates [e.g., *Westerhold et al.*, 2008, 2009].

[26] Recently, *Jaramillo et al.* [2010] obtained a $^{238}\text{U}/^{206}\text{Pb}$ date of 56.09 ± 0.13 Ma (total uncertainty) on zircons from a felsic pyroclastic tuff from a coastal plain Late Paleocene–early Eocene section in Venezuela (Riecito Mache section). This pyroclastic tuff is at a level that records a negative CIE that is inferred to represent the PETM, and therefore inferentially constrains the P-E boundary to ~56.3 Ma [*Jaramillo et al.*, 2010]. This date is ~400–500 kyr older than our age for the P-E boundary. The zircons utilized to derive this date were extracted from a sample described as tuffaceous sandstone [*Jaramillo et al.*, 2010, Figure S3]. It is therefore possible that fluvial reworking of detrital zircons from an eruption ~56.1 Ma could account for the discrepancy between the Spitsbergen and Venezuelan P-E boundary ages. In addition, the identification of the PETM CIE at the

Riecito Mache section is complicated by $\delta^{13}\text{C}_{\text{TOC}}$ records with a high degree of scatter, and therefore an alternative explanation is that the dated tuffaceous sandstone was not deposited within the PETM CIE.

[27] The PETM CIE in Spitsbergen is firmly identified by $\delta^{13}\text{C}_{\text{TOC}}$ records together with the *Apectodinium* acme (Figure 2) [e.g., Crouch *et al.*, 2001; Sluijs and Brinkhuis, 2009], and dinocyst morphotype *Apectodinium augustum*, which only occurs within the PETM interval [e.g., Luterbacher *et al.*, 2004]. Given the accuracy of the U-Pb (zircon) system by isotope dilution, the context of the dated sample within the PETM CIE and the proximity of the dated horizon to the P-E boundary, we consider our age range of 55.728–55.964 Ma for the P-E boundary from Spitsbergen to be the most accurate radioisotopic age estimate. Our age range for the boundary is within error of age option 2 of Westerhold *et al.* [2007, 2008] for the same horizon. The numerical age for the P-E boundary (equivalent to the PETM onset) must fall within one of the age options proposed by Westerhold *et al.* [2007, 2008] in order to maintain the phase relationship of the 405 kyr eccentricity cycle between astronomical solutions and records of the same cycle extracted from ODP Site 1262 [Röhl *et al.*, 2007; Westerhold *et al.*, 2007, 2008]. Therefore, our age for the P-E boundary substantiates age option 2 of Westerhold *et al.* [2007, 2008] is the correct option, giving a numerical age of ~55.93 Ma for the boundary.

4.2. On the Age of the K-Pg Boundary

[28] Radioisotopic constraints at the K-Pg boundary (e.g., single crystal $^{40}\text{Ar}/^{39}\text{Ar}$ sanidine dates from the IrZ-Coal bentonite, Hell Creek Formation, Montana [Swisher *et al.*, 1993]) and immediately overlying the P-E boundary (Spitsbergen, this study) now bracket Paleocene time, constraining its duration. However, at present uncertainty in the numerical age of the monitor standards used in the $^{40}\text{Ar}/^{39}\text{Ar}$ studies that constrain the K-Pg boundary (see section 1) result in uncertainties on the order of ~600 kyr or greater [Kuiper *et al.*, 2008; Channell *et al.*, 2010; Renne *et al.*, 2010] which precludes the accurate determination of the number of 405 kyr cycles within the Paleocene. Given our high-precision and high-accuracy constraint for the P-E boundary we suggest that the uncertainty of the numerical age of the K-Pg boundary now represents the most substantial source of uncertainty for constraining the duration of the Paleocene. However, an alternative way to derive the age

of the K-Pg boundary is to use our P-E boundary age together with the duration of the Paleocene Epoch derived from cyclostratigraphic studies.

[29] Such cyclostratigraphic analyses of early Paleogene successions from ODP Legs 198 (Shatsky Rise, NW Pacific Ocean) and 208 (Walvis Ridge, SE Atlantic Ocean), together with ODP sites 1001 (Nicaragua Basin), 1051 (Blake Nose) and the Zumaia outcrop section (Basque Basin, Spain), led to the development of an age model for the Paleocene where the K-Pg and P-E boundaries were separated by twenty-four 405 kyr eccentricity cycles giving a duration of 9.720 Myr [Westerhold *et al.*, 2008]. However, recent analysis of the Zumaia outcrop section [Kuiper *et al.*, 2008], implies that an additional 405 kyr eccentricity cycle (relative to Westerhold *et al.* [2008]) is present in the Paleocene epoch. A revised analysis of the Fe and magnetic susceptibility records from ODP Site 1263 has also suggested twenty-five 405 kyr eccentricity cycles are present in the Paleocene [Hilgen *et al.*, 2010]. If we assume that the most recent cyclostratigraphic studies for the duration of the Paleocene are accurate (twenty-five 405 kyr cycles [Kuiper *et al.*, 2008; Hilgen *et al.*, 2010]), this would indicate a duration of 10.125 Myr for the Paleocene epoch. This duration combined with our age range of 55.728–55.964 Ma for the P-E boundary predicts an age of ~66 Ma for the K-Pg boundary.

4.3. Implications for the PETM Trigger Mechanism

[30] Our new age for the P-E boundary allows us to investigate the relationship between the PETM and potential forcing mechanisms. It has been proposed that insolation maxima during the peak of both short (~100 kyr) and long (405 kyr) eccentricity cycles may have resulted in warmer water conditions, triggering the dissociation of methane hydrates on the seafloor, and thus generating hyperthermal events such as the PETM [Cramer *et al.*, 2003; Lourens *et al.*, 2005; Sluijs *et al.*, 2007]. However, Westerhold *et al.* [2007] argued that the PETM occurred on the falling limb of a 405 kyr eccentricity cycle, based on records of this cycle extracted from ODP Site 1262. Here, we plot our age range of 55.728–55.964 Ma for the P-E boundary (equivalent to the PETM CIE onset) against the astronomical solution of Laskar *et al.* [2004] to illustrate the relationship between the PETM onset age and 405 kyr eccentricity forcing (Figure 10). Orbital models have illustrated that the 405 kyr eccentricity phase is stable over the entire Paleo-

gene interval [Laskar *et al.*, 2004], which validates our approach, although the relative cycle-to-cycle amplitude is less certain due to the chaotic nature of the solar system. The total uncertainty for the age of the PETM onset from Spitsbergen illustrates that the PETM was not initiated on the peak of a 405 kyr cycle (Figure 10). In addition, it has been argued that the PETM onset age must fall within one of the age options proposed by Westerhold *et al.* [2007, 2008] in order to maintain the phase relationship of the 405 kyr eccentricity cycle between astronomical solutions and records of the same cycle extracted from ODP Site 1262 [Röhl *et al.*, 2007; Westerhold *et al.*, 2007, 2008]. Given our age range is within error of astronomical age option 2 (Figure 10), our results are consistent with the hypothesis that the onset of the PETM occurred on the falling limb of a 405 kyr eccentricity cycle [Westerhold *et al.*, 2007]. Conversely, cyclostratigraphic studies of geological data sets have consistently placed ETM2 (equivalent to the Elmo event of Lourens *et al.* [2005] or to the event H1 of Cramer *et al.* [2003]), ETM3 (or the X event of Zachos *et al.* [2004] or the event K of Cramer *et al.* [2003]) and other potential hyperthermals (negative CIEs of Cramer *et al.* [2003]) either on the maxima of both 100 and 405 kyr cycles [Lourens *et al.*, 2005; Galeotti *et al.*, 2010] or with ETM2 at a 100 kyr eccentricity peak on the rising limb of a 405 kyr eccentricity cycle [Westerhold *et al.*, 2007; Westerhold and Röhl, 2009; Zachos *et al.*, 2010], consistent with orbital forcing as a common trigger mechanism. Therefore, the occurrence of the PETM on the falling limb of a 405 kyr eccentricity cycle supports the hypothesis that the event required a different trigger mechanism when compared to other early Eocene hyperthermals [Zachos *et al.*, 2010].

[31] It has also been proposed that the PETM may have been triggered by the injection of volcanic sills into organic-rich sediments in the North Atlantic, generating methane and/or carbon dioxide via contact metamorphism, with outgassing through hydrothermal vent systems [Svensen *et al.*, 2004, 2010; Storey *et al.*, 2007]. If correct, it would be expected that the emplacement of these sills occurred immediately prior to the onset of the PETM. Recent estimates for the emplacement of sills on the Vøring Plateau (55.6 ± 0.3 and 56.3 ± 0.4 Ma [Svensen *et al.*, 2010]) and for the eruption of mid-ocean ridge basalt-like flows in the North Atlantic (55.5 ± 0.3 Ma [Storey *et al.*, 2007]) are within error of our new age for the onset of the PETM. However, given the low uncertainty on our age for the PETM

onset, age estimates with equivalent uncertainties are required for igneous units in the North Atlantic, in order to fully test the hypothesis that volcanism was responsible for the release of the isotopically light carbon which gave rise to the PETM.

5. Conclusions

[32] Our combined chemostratigraphic and biostratigraphic analysis enables the PETM to be recognized at two localities in the Central Basin of Spitsbergen, and demonstrates that two coeval bentonite layers occur within the PETM CIE at both localities. By integrating cyclostratigraphic data sets with radioisotopic dating ($^{238}\text{U}/^{206}\text{Pb}$, zircon) of the PETM CIE, we derive similar numerical ages for the P-E boundary based on two different options for the interpretation of the cyclostratigraphic data. This approach yields a total uncertainty for the P-E boundary (equivalent to the PETM CIE onset age) between 55.728 and 55.964 Ma, which is within error of astronomical age option 2 [Westerhold *et al.*, 2007, 2008]. Combined with models of the duration of the Paleocene spanning twenty-five 405 kyr cycles [Kuiper *et al.*, 2008; Hilgen *et al.*, 2010], our new age range for the boundary predicts that the numerical age of the K-Pg boundary is ~66 Ma. Furthermore, the new age for the P-E boundary (PETM CIE onset age) provides additional constraints on the trigger mechanism for the PETM. Comparing our age range for the PETM CIE onset with the Laskar *et al.* [2004] orbital solution indicates that the event was not initiated on a 405 kyr eccentricity peak. Furthermore, our age range is within error of astronomical age option 2 of Westerhold *et al.* [2007, 2008], consistent with the hypothesis that the onset of the PETM occurred on the falling limb of a 405 kyr eccentricity cycle [Westerhold *et al.*, 2007]. Conversely, other early Eocene hyperthermals have been inferred to occur on eccentricity maxima (or with ETM2 on the rising limb of a 405 kyr cycle) consistent with orbital forcing as a common trigger mechanism. Our results thus suggest that the PETM was triggered by a mechanism different from that proposed for the later Eocene hyperthermals.

Acknowledgments

[33] Store Norske Spitsbergen Grubekompani (SNSK) kindly allowed access and sampling of core BH9/05, carried out by the WUN pACE Group in 2007 and 2008. WUN pACE members Tim White and Malte Jochmann provided invaluable logistical help, and the authors also acknowledge the exertions

of the 2008 sampling party consisting of Henning Dypvik, Jenő Nagy, Lars Riber, and David Jargvoll. John Hurley of Niton UK provided invaluable assistance with the Niton UK XRF Scanner. Mark Schmitz, Frits Hilgen, and an anonymous reviewer provided thoughtful and thorough reviews which dramatically improved the paper. AJCs' research was supported by NERC CASE Ph.D. studentship NE/F006721/1, in conjunction with Shell UK. U-Pb (zircon) analyses were supported by NIGFSC grant IP/1157/1109. HP's research was supported by a Philip Leverhulme Prize.

References

- Abdul Aziz, H., F. J. Hilgen, G. M. Van Luijk, A. Sluijs, M. J. Kraus, J. M. Pares, and P. D. Gingerich (2008), Astronomical climate control on the paleosol stacking patterns in the upper Paleocene–lower Eocene Willwood Formation, Bighorn Basin, Wyoming, *Geology*, **36**, 531–534, doi:10.1130/G24734A.1.
- Agnini, C., P. Macri, J. Backman, H. Brinkhuis, E. Fornaciari, L. Giusberti, V. Luciani, D. Rio, A. Sluijs, and F. Speranza (2009), An early Eocene carbon cycle perturbation at ~52.5 Ma in the Southern Alps: Chronology and biotic response, *Paleoceanography*, **24**, PA2209, doi:10.1029/2008PA001649.
- Bains, S., R. M. Corfield, and R. D. Norris (1999), Mechanisms of climate warming at the end of the Paleocene, *Science*, **285**, 724–727.
- Bailey, R. J. (2009), Cyclostratigraphic reasoning and orbital time calibration, *Terra Nova*, **21**, 340–351, doi:10.1111/j.1365-3121.2009.00890.x.
- Bijl, P. K., S. Schouten, A. Sluijs, G.-J. Reichert, J. C. Zachos, and H. Brinkhuis (2009), Early Palaeogene temperature evolution of the southwest Pacific Ocean, *Nature*, **461**, 776–779, doi:10.1038/nature08399.
- Blythe, A. E., and K. L. Kleinspehn (1998), Tectonically versus climatically driven Cenozoic exhumation of the Eurasian plate margin, Svalbard: Fission track analyses, *Tectonics*, **17**, 621–639, doi:10.1029/98TC01890.
- Bruhn, R., and R. Steel (2003), High-resolution sequence stratigraphy of a clastic foredeep succession (Paleocene, Spitsbergen): An example of peripheral-bulge-controlled depositional architecture, *J. Sediment. Res.*, **73**, 745–755, doi:10.1306/012303730745.
- Channell, J. E. T., D. A. Hodell, B. S. Singer, and C. Xuan (2010), Reconciling astrochronological and ⁴⁰Ar/³⁹Ar ages for the Matuyama–Brunhes boundary and late Matuyama Chron, *Geochem. Geophys. Geosyst.*, **11**, Q0AA12, doi:10.1029/2010GC003203.
- Condon, D., B. Schoene, S. Bowring, R. Parrish, N. McLean, S. Noble, and Q. Crowley (2007), EARTHTIME: isotopic tracers and optimized solutions for high-precision U–Pb ID–TIMS geochronology, *Eos Trans. AGU*, **88**(52), Fall Meet. Suppl., Abstract V41E-06.
- Cramer, B. S., J. D. Wright, D. V. Kent, and M. Aubry (2003), Orbital climate forcing of $\delta^{13}\text{C}$ excursions in the late Paleocene–early Eocene (chrons C24n–C25n), *Paleoceanography*, **18**(4), 1097, doi:10.1029/2003PA000909.
- Crouch, E. M., C. Heilmann-Clausen, H. Brinkhuis, H. E. G. Morgans, K. M. Rogers, H. Egger, and B. Schmitz (2001), Global dinoflagellate event associated with the late Paleocene Thermal Maximum, *Geology*, **29**, 315–318, doi:10.1130/0091-7613(2001)029<0315:GDEAWT>2.0.CO;2.
- Cui, Y. (2010), Carbon addition during the Paleocene–Eocene thermal maximum: Model inversion of a new, high-resolution carbon isotope record from Svalbard, unpublished M.S. thesis, *Dep. of Geosci.*, Pennsylvania State Univ., University Park, Pa.
- Dallmann, W. K., P. S. Midbø, A. Nøttvedt, and R. J. Steel (1999), Tertiary lithostratigraphy, in *Lithostratigraphic Lexicon of Svalbard*, edited by W. K. Dallmann, pp. 215–263, Norsk Polarinstitutt, Tromsø, Norway.
- Dettinger, M. D., M. Ghil, C. M. Strong, W. Weibel, and P. Yiou (1995), Software expedites singular-spectrum analysis of noisy time series, *Eos Trans. AGU*, **76**, 12.
- Dickens, G. R., J. R. O'Neil, D. K. Rea, and R. M. Owen (1995), Dissociation of oceanic methane hydrate as a cause of the carbon isotope excursion at the end of the Paleocene, *Paleoceanography*, **10**, 965–971, doi:10.1029/95PA02087.
- Dickens, G. R., M. M. Castillo, and J. C. G. Walker (1997), A blast of gas in the latest Paleocene: Simulating first order effects of massive dissociation of oceanic methane hydrate, *Geology*, **25**, 259–262, doi:10.1130/0091-7613(1997)025<0259:ABOGIT>2.3.CO;2.
- Dupuis, C., M.-P. Aubry, E. Steurbaut, W. A. Berggren, K. Ouda, R. Magioncalda, B. S. Cramer, D. V. Kent, R. P. Speijer, and C. Heilmann-Clausen (2003), The Dababiya quarry section: Lithostratigraphy, clay mineralogy, geochemistry and paleontology, *Micropaleontology*, **49**, 41–59, doi:10.2113/49.Suppl.1.41.
- Dypvik, H., L. Riber, F. Burca, D. Røther, D. Jargvoll, J. Nagy, and M. Jochmann (2011), The Paleocene–Eocene thermal maximum (PETM) in Svalbard–clay mineral and geochemical signals, *Palaeogeogr. Palaeoclimatol. Palaeoecol.*, in press.
- Farley, K. A., and S. F. Eltgroth (2003), An alternative age model for the Paleocene–Eocene thermal maximum using extraterrestrial ³He, *Earth Planet. Sci. Lett.*, **208**, 135–148, doi:10.1016/S0012-821X(03)00017-7.
- Fensome, R. A., and G. L. Williams (2004), The Lentin and Williams Index of Fossil Dinoflagellates–2004 Edition, *Am. Assoc. of Stratigr. Palynol., Contrib. Ser.*, **42**, 909 pp.
- Galeotti, S., S. Krishnan, M. Pagani, L. Lanci, A. Gaudio, J. C. Zachos, S. Monechi, G. Morelli, and L. Lourens (2010), Orbital chronology of early Eocene hyperthermals from the Contessa Road section, central Italy, *Earth Planet. Sci. Lett.*, **290**, 192–200, doi:10.1016/j.epsl.2009.12.021.
- Ghil, M., et al. (2002), Advanced spectral methods for climatic time series, *Rev. Geophys.*, **40**(1), 1003, doi:10.1029/2000RG000092.
- Harding, I. C., et al. (2011), Sea level and salinity fluctuations during the Palaeocene/Eocene thermal maximum in Arctic Spitsbergen, *Earth Planet. Sci. Lett.*, **303**, 97–107, doi:10.1016/j.epsl.2010.12.043.
- Harland, W. (1997), Palaeogene history of Svalbard, in *The Geology of Svalbard, Mem. Geol. Soc. London*, vol. 17, edited by B. Harland, pp. 388–417.
- Helland-Hansen, W. (1990), Sedimentation in Paleogene Foreland Basin, Spitsbergen, *Am. Assoc. Pet. Geol. Bull.*, **74**, 260–272.
- Hilgen, F. J. (2008), Recent progress in the standardization and calibration of the Cenozoic Time Scale, *Newsl. Stratigr.*, **43**, 15–22.
- Hilgen, F. J., K. F. Kuiper, and L. J. Lourens (2010), Evaluation of the astronomical time scale for the Paleocene and earliest Eocene, *Earth Planet. Sci. Lett.*, **300**, 139–151, doi:10.1016/j.epsl.2010.09.044.
- Jaffey, A. H., K. F. Flynn, L. E. Glendenin, W. C. Bentley, and A. M. Essling (1971), Precision measurement of half-lives

- and specific activities of ^{235}U and ^{238}U , *Phys. Rev. C*, **4**, 1889–1906, doi:10.1103/PhysRevC.4.1889.
- Jaramillo, C., et al. (2010), Effects of rapid global warming at the Paleocene-Eocene boundary on Neotropical vegetation, *Science*, **330**, 957–961, doi:10.1126/science.1193833.
- John, C. M., S. M. Bohaty, J. C. Zachos, A. Sluijs, S. Gibbs, H. Brinkhuis, and T. Bralower (2008), North American continental margin records of the Palaeocene-Eocene Thermal Maximum: Implications for global carbon and hydrological cycling, *Paleoceanography*, **23**, PA2217, doi:10.1029/2007PA001465.
- Kellogg, H. E. (1975), Tertiary stratigraphy and tectonism in Svalbard and continental drift, *Am. Assoc. Pet. Geol. Bull.*, **59**, 465–485.
- Kennett, J., and L. Stott (1991), Abrupt deep-sea warming, palaeoceanographic changes and benthic extinctions at the end of the Palaeocene, *Nature*, **353**, 225–229, doi:10.1038/353225a0.
- Kuiper, K. F., A. Deino, F. J. Hilgen, W. Krijgsman, P. R. Renne, and J. R. Wijbrans (2008), Synchronizing rock clocks of Earth history, *Science*, **320**, 500–504, doi:10.1126/science.1154339.
- Laskar, J. (1999), The limits of Earth orbital calculations for geological timescale use, *Philos. Trans. R. Soc. A*, **357**, 1735–1759, doi:10.1098/rsta.1999.0399.
- Laskar, J., P. Robutel, F. Joutel, M. Gastineau, A. C. M. Correia, and B. Levrard (2004), A long-term solution for the insolation quantities of the Earth, *Astron. Astrophys.*, **428**, 261–285, doi:10.1051/0004-6361:20041335.
- Lourens, L. J., A. Sluijs, D. Kroon, J. C. Zachos, E. Thomas, U. Röhl, J. Bowles, and I. Raffi (2005), Astronomical pacing of late Palaeocene to early Eocene global warming events, *Nature*, **435**, 1083–1087, doi:10.1038/nature03814.
- Ludwig, K. R. (1991), Isoplot—A plotting and regression program for radiogenic isotope data, *U.S. Geol. Surv. Open File Rep.*, 91–445.
- Luterbacher, H. P., et al. (2004), The Paleogene Period, in *A Geologic Time Scale 2004*, edited by F. M. Gradstein, J. G. Ogg, and A. G. Smith, pp. 384–408, Cambridge Univ. Press, Cambridge, UK.
- Mattinson, J. M. (2005), Zircon U-Pb chemical abrasion (“CA-TIMS”) method: Combined annealing and multi-step partial dissolution analysis for improved precision and accuracy of zircon ages, *Chem. Geol.*, **220**, 47–66, doi:10.1016/j.chemgeo.2005.03.011.
- McCarren, H., E. Thomas, T. Hasegawa, U. Röhl, and J. C. Zachos (2008), Depth dependency of the Paleocene-Eocene carbon isotope excursion: Paired benthic and terrestrial biomarker records (Ocean Drilling Program Leg 208, Walvis Ridge), *Geochem. Geophys. Geosyst.*, **9**, Q10008, doi:10.1029/2008GC002116.
- Mosar, J., T. H. Torsvik, and BAT team (2002), Opening of the Norwegian and Greenland Seas: Plate tectonics in Mid Norway since the Late Permian, in *BATLAS—Mid Norway Plate Reconstructions Atlas With Global and Atlantic Perspectives*, edited by E. A. Eide, pp. 48–59, Geol. Surv. of Norway, Trondheim, Norway.
- Müller, R. D., and R. F. Spielhagen (1990), Evolution of the Central Basin of Spitsbergen: Towards a synthesis of sediment and plate tectonic history, *Palaeogeogr. Palaeoclimatol. Palaeoecol.*, **80**, 153–172, doi:10.1016/0031-0182(90)90127-S.
- Murphy, B. H., K. A. Farley, and J. C. Zachos (2010), An extraterrestrial ^3He -based timescale for the Paleocene-Eocene thermal maximum (PETM) from Walvis Ridge, IODP Site 1266, *Geochim. Cosmochim. Acta*, **74**, 5098–5108, doi:10.1016/j.gca.2010.03.039.
- Nicolo, M. J., G. R. Dickens, C. J. Hollis, and J. C. Zachos (2007), Multiple early Eocene hyperthermals: Their sedimentary expression on the New Zealand continental margin and in the deep sea, *Geology*, **35**, 699–702, doi:10.1130/G23648A.1.
- Paillard, D., L. Labeyrie, and P. Yiou (1996), Macintosh program performs time series analysis, *Eos Trans. AGU*, **77**, 379, doi:10.1029/96EO00259.
- Pälike, H. (2005), Orbital variation (including Milankovitch cycles), in *Encyclopedia of Geology*, vol. 1, edited by R. C. Selley, L. R. M. Cocks, and I. R. Plimer, pp. 410–421, Elsevier, Oxford, U. K., doi:10.1016/B0-12-369396-9/00123-4.
- Pälike, H., and F. Hilgen (2008), Rock clock synchronization, *Nat. Geosci.*, **1**, 282, doi:10.1038/ngeo197.
- Pälike, H., J. Laskar, and N. J. Shackleton (2004), Geologic constraints on the chaotic diffusion of the solar system, *Geology*, **32**, 929–932, doi:10.1130/G20750.1.
- Panchuk, K., A. Ridgwell, and L. Kump (2008), Sedimentary response to Paleocene-Eocene Thermal Maximum Carbon release: A model-data comparison, *Geology*, **36**, 315–318, doi:10.1130/G24474A.1.
- Pearson, P. N., B. E. van Dongen, C. J. Nicholas, R. D. Pancost, S. Schouten, J. M. Singano, and B. S. Wade (2007), Stable warm tropical climate through the Eocene Epoch, *Geology*, **35**, 211–214, doi:10.1130/G23175A.1.
- Renne, P. R., C. C. Swisher, A. L. Deino, D. B. Karner, T. L. Owens, and D. J. DePaolo (1998), Intercalibration of standards, absolute ages and uncertainties in $^{40}\text{Ar}/^{39}\text{Ar}$ dating, *Chem. Geol.*, **145**, 117–152, doi:10.1016/S0009-2541(97)00159-9.
- Renne, P. R., R. Mundil, G. Balco, K. Min, and K. R. Ludwig (2010), Joint determination of ^{40}K decay constants and $^{40}\text{Ar}^*/^{40}\text{K}$ for the Fish Canyon sanidine standard, and improved accuracy for $^{40}\text{Ar}/^{39}\text{Ar}$ geochronology, *Geochim. Cosmochim. Acta*, **74**, 5349–5367, doi:10.1016/j.gca.2010.06.017.
- Röhl, U., T. Westerhold, T. J. Bralower, and J. C. Zachos (2007), On the duration of the Paleocene-Eocene Thermal Maximum (PETM), *Geochem. Geophys. Geosyst.*, **8**, Q12002, doi:10.1029/2007GC001784.
- Schärer, U. (1984), The effect of initial ^{230}Th disequilibrium on young U–Pb ages: The Makalu case, Himalaya, *Earth Planet. Sci. Lett.*, **67**, 191–204, doi:10.1016/0012-821X(84)90114-6.
- Schmitz, M. D., and B. Schoene (2007), Derivation of isotope ratios, errors and error correlations for U–Pb geochronology using ^{205}Pb – ^{235}U –(^{233}U)-spiked isotope dilution thermal ionization mass spectrometric data, *Geochem. Geophys. Geosyst.*, **8**, Q08006, doi:10.1029/2006GC001492.
- Schoene, B., J. Guex, A. Bartolini, U. Schaltegger, and T. J. Blackburn (2010), Correlating the end-Triassic mass extinction and flood basalt volcanism at the 100 ka level, *Geology*, **38**, 387–390, doi:10.1130/G30683.1.
- Sláma, J., et al. (2008), Plešovice zircon—A new natural reference material for U–Pb and Hf isotopic microanalysis, *Chem. Geol.*, **249**, 1–35, doi:10.1016/j.chemgeo.2007.11.005.
- Sluijs, A., and H. Brinkhuis (2009), A dynamic climate and ecosystem state during the Paleocene-Eocene Thermal Maximum: Inferences from dinoflagellate cyst assemblages on the New Jersey Shelf, *Biogeosciences*, **6**, 1755–1781, doi:10.5194/bg-6-1755-2009.

- Sluijs, A., et al. (2006), Subtropical Arctic Ocean temperatures during the Palaeocene-Eocene Thermal Maximum, *Nature*, 441, 610–613, doi:10.1038/nature04668.
- Sluijs, A., G. J. Bowen, H. Brinkhuis, L. J. Lourens, and E. Thomas (2007), The Palaeocene-Eocene Thermal Maximum super greenhouse: Biotic and geochemical signatures, age models and mechanisms of global change, in *Deep-Time Perspectives on Climate Change: Marrying the Signal from Computer Models and Biological Proxies*, edited by M. Williams et al., *Micropalaeontological Soc. Spec. Publ.*, 323–349.
- Sluijs, A., U. Röhl, S. Schouten, H. Brumsack, F. Sangiorgi, J. S. Sinninghe Damsté, and H. Brinkhuis (2008), Arctic late Paleocene–early Eocene paleoenvironments with special emphasis on the Paleocene-Eocene Thermal Maximum (Lomonosov Ridge, Integrated Ocean Drilling Program Expedition 302), *Paleoceanography*, 23, PA1S11, doi:10.1029/2007PA001495.
- Steel, R. J., J. Gjølberg, W. Helland-Hansen, K. Kleinspehn, A. Nøttvedt, and M. Rye-Larsen (1985), The Tertiary strike-slip basins and orogenic belt of Spitsbergen, in *Strike-Slip Deformation, Basin Formation, and Sedimentation*, edited by K. T. Biddle and N. Christie-Blick, *Soc. Econ. Paleontol. Mineral. Spec. Publ.*, 37, 339–359, doi:10.2110/pec.85.37.0339.
- Stockmarr, J. (1971), Tablets with spores used in absolute pollen analysis, *Pollen et Spores*, 13, 615–621.
- Storey, M., R. A. Duncan, and C. C. Swisher III (2007), Paleocene-Eocene thermal maximum and the opening of the northeast Atlantic, *Science*, 316, 587–589, doi:10.1126/science.1135274.
- Svensen, H., S. Planke, A. Mørth-Sørensen, B. Jamveit, R. Myklebust, T. Eidem, and S. Rey (2004), Release of methane from a volcanic basin as a mechanism for initial Eocene global warming, *Nature*, 429, 542–545, doi:10.1038/nature02566.
- Svensen, H., S. Planke, and F. Corfu (2010), Zircon dating ties NE Atlantic sill emplacement to initial Eocene global warming, *J. Geol. Soc.*, 167, 433–436, doi:10.1144/0016-76492009-125.
- Swisher, C. C., L. Dingus, and R. F. Butler (1993), $^{40}\text{Ar}/^{39}\text{Ar}$ dating and magnetostratigraphic correlation of the terrestrial Cretaceous–Paleogene boundary and Puerco Mammal Age, Hell Creek–Tullock formations, eastern Montana, *Can. J. Earth Sci.*, 30, 1981–1996.
- Thomson, D. J. (1982), Spectrum estimation and harmonic analysis, *Proc. IEEE*, 70, 1055–1096, doi:10.1109/PROC.1982.12433.
- Torrence, C., and G. P. Compo (1998), A practical guide to wavelet analysis, *Bull. Am. Meteorol. Soc.*, 79, 61–78, doi:10.1175/1520-0477(1998)079<0061:APGTWA>2.0.CO;2.
- Tripathi, A., and H. Elderfield (2005), Deep-sea temperature and circulation changes at the Paleocene-Eocene thermal maximum, *Science*, 308, 1894–1898, doi:10.1126/science.1109202.
- Uroza, C. A., and R. J. Steel (2008), A highstand shelf-margin delta system from the Eocene of West Spitsbergen, Norway, *Sediment. Geol.*, 203, 229–245, doi:10.1016/j.sedgeo.2007.12.003.
- Varadi, F., B. Runnegar, and M. Ghil (2003), Successive refinements in long-term integrations of planetary orbits, *Astrophys. J.*, 592, 620–630, doi:10.1086/375560.
- Weedon, G. (2003), *Time-Series Analysis and Cyclostratigraphy: Examining stratigraphic records of environmental cycles*, Cambridge Univ. Press, Cambridge, U. K., doi:10.1017/CBO9780511535482.
- Westerhold, T., and U. Röhl (2009), High resolution cyclostratigraphy of the early Eocene—New insights into the origin of the Cenozoic cooling trend, *Clim. Past*, 5, 309–327, doi:10.5194/cp-5-309-2009.
- Westerhold, T., U. Röhl, J. Laskar, I. Raffi, J. Bowles, L. J. Lourens, and J. C. Zachos (2007), On the duration of magnetochrons C24r and C25n and the timing of early Eocene global warming events: Implications from the Ocean Drilling Program Leg 208 Walvis Ridge depth transect, *Paleoceanography*, 22, PA2201, doi:10.1029/2006PA001322.
- Westerhold, T., U. Röhl, I. Raffi, E. Fornaciari, S. Monechi, V. Reale, J. Bowles, and H. F. Evans (2008), Astronomical calibration of Paleocene time, *Palaeogeogr. Palaeoclimatol. Palaeoecol.*, 257, 377–403, doi:10.1016/j.palaeo.2007.09.016.
- Westerhold, T., U. Röhl, H. K. McCarren, and J. C. Zachos (2009), Latest on the absolute age of the Paleocene-Eocene thermal maximum (PETM): New insights from exact stratigraphic position of key ash layers +19 and –17, *Earth Planet. Sci. Lett.*, 287, 412–419, doi:10.1016/j.epsl.2009.08.027.
- Wing, S., H. Bao, and P. L. Koch (2000), An early Eocene cool period? Evidence for continental cooling during the warmest part of the Cenozoic, in *Warm Climates in Earth History*, edited B. T. Huber, K. G. MacLeod, and S. L. Wing, pp. 197–237, Cambridge Univ. Press, Cambridge, U. K.
- Zachos, J. C., M. Pagani, L. Sloan, E. Thomas, and K. Billups (2001), Trends, rhythms, and aberrations in global climate 65 Ma to present, *Science*, 292, 686–693, doi:10.1126/science.1059412.
- Zachos, J. C., M. W. Wara, and S. Bohaty (2003), A transient rise in tropical sea surface temperature during the Paleocene-Eocene Thermal Maximum, *Science*, 302, 1551–1554, doi:10.1126/science.1090110.
- Zachos, J. C., et al. (2004), *Proceedings of the Ocean Drilling Program, Initial Reports*, Ocean Drill. Program, College Station, Tex.
- Zachos, J. C., et al. (2005), Rapid acidification of the ocean during the Paleocene-Eocene Thermal Maximum, *Science*, 308, 1611–1615, doi:10.1126/science.1109004.
- Zachos, J. C., G. R. Dickens, and R. E. Zeebe (2008), An early Cenozoic perspective on greenhouse warming and carbon-cycle dynamics, *Nature*, 451, 279–283, doi:10.1038/nature06588.
- Zachos, J. C., H. McCarren, B. Murphy, U. Röhl, and T. Westerhold (2010), Tempo and scale of late Paleocene and early Eocene carbon isotope cycles: Implications for the origin of hyperthermals, *Earth Planet. Sci. Lett.*, 299, 242–249, doi:10.1016/j.epsl.2010.09.004.
- Zeebe, R. E., J. C. Zachos, and G. R. Dickens (2009), Carbon dioxide forcing alone insufficient to explain Palaeocene-Eocene Thermal Maximum warming, *Nat. Geosci.*, 2, 576–580.